On the analysis of experimental signals for evidence of deterministic chaos

Helvetica Physica Acta, Vol. 60 (1987) 510–551

0018–0238/87/040510–42$1.50 + 0.20/0

On the analysis of experimental signals for evidence of deterministic chaos

By C. W. Simm, M. L. Sawley[1]), F. Skiff and A. Pochelon

Centre de Recherches en Physique des Plasmas, Association Euratom, Confédération Suisse, Ecole Polytechnique Fédérale de Lausanne, 21, Av. des Bains, CH-1007 Lausanne/Switzerland

(8. I. 1987)

Abstract. The application of the analysis methods of dissipative chaotic systems to experimental signals is considered. After a brief review of definitions and the available measures of chaos, comments are made on some of the algorithms available to analyse statistically chaotic systems. In particular, the Grassberger–Procaccia algorithm for calculating the correlation dimension is seen to be relatively well-suited for application to experimental signals. Several cautions regarding the use of this algorithm, however, are elaborated through examples involving both numerically and experimentally produced data. It is found that, despite the complications produced by extrinsic noise and finite discrete data samples, it is possible to obtain consistent results.

1. Introduction

As new concepts and techniques appear in the study of deterministic chaos in dissipative systems, it is natural to look for their application to physical systems. In particular, since it has become clear that simple (in appearance) non-linear model systems often have very complex dynamics, one might ask if the apparently complex behaviour of certain physical systems may be adequately described by a simple non-linear model. The various quantities used to characterize dynamical chaos provide a first step toward the resolution of this question. This first question is: can the chaotic dynamics of a simple system (small number of degrees of freedom) be distinguished from that of an inherently complex system (one with dynamics which fill a large dimensional phase space) through observation of a single variable? If the answer is in the affirmative, the application of the characterizations of dynamical chaos to experimental systems may be of interest.

In this paper, consideration is given to some of the problems involved in the application of the measures of chaos used in the study of model systems to experimental data. Section 2 gives a brief review of some basic definitions before the characterizations commonly used for chaos are presented (Section 3). The Kolmogorov entropy, Lyapunov exponents, and generalized dimensions are

[1]) Present address: School of Physics, The University of Sydney, Australia.

described and some interrelationships are noted. The problem of reconstructing and characterizing an attractor from discrete data is considered with regard to the available algorithms. The Grassberger-Procaccia algorithm, considered as the most applicable, is described in Section 4. The role of various parameters is described, and some comments are made on their selection and on the interpretation of the results. Section 5 provides some mathematical examples which serve as test cases for the algorithm, and considers the influence of noise and filtering. Section 6 presents the numerical analysis of a model system (the bipolar motor), an experimental study of which is reported in Section 7. For this case, a comparison between theory and experiment is possible. Section 8 describes the application of the dimensional analysis to fluctuation measurements of a tokamak plasma, while Section 9 contains some concluding comments.

Readers already familiar with the basic concepts of chaotic dynamical systems may wish to begin with Section 4.

2. Definitions

Dynamical systems may be conveniently analysed by means of a multi-dimensional phase space, in which to any state of a system at any time corresponds a point. Therefore, to any motion of a system corresponds an orbit or trajectory.

Given a set of initial conditions occupying a finite volume in phase space, Liouville's theorem asserts the conservation in time of this volume for Hamiltonian ('conservative') dynamical systems. The theorem does not hold for dissipative systems, for which there is generally a contraction of volume in phase space.

2.1. *Attractors*

If the asymptotic behaviour of a dissipative dynamical system is such that the volume of initial conditions contracts to some subset of the phase space, then this subset is called an 'attractor' [1, 2, 3]. The following examples illustrate this behaviour [4, 5].

2.1.1. *A zero-dimensional attractor.* The damped harmonic oscillator, described by the equation

$$\frac{d^2\theta}{dt^2} + \gamma \frac{d\theta}{dt} + \omega^2 \theta = 0 \tag{2.1}$$

where γ is the damping factor, is a simple example of a zero-dimensional attractor. A typical trajectory in its phase space $(\theta, \dot{\theta})$ is shown in Fig. 1.

The trajectories corresponding to any set of initial conditions in the two-dimensional phase space approach the point $\theta = \dot{\theta} = 0$. Thus, the attractor is zero-dimensional, corresponding to a time-independent solution.

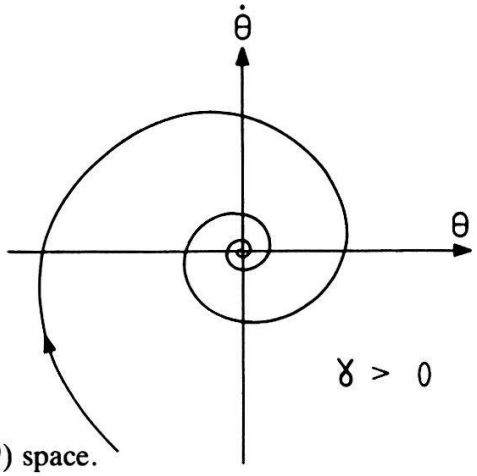

Figure 1
A typical trajectory of the damped harmonic oscillator in $(\theta, \dot{\theta})$ space.

2.1.2. *A one-dimensional attractor.* The Van der Pol oscillator, a simple model with a one-dimensional attractor, is obtained by introducing non-linear damping in equation (2.1):

$$\frac{d^2\theta}{dt^2} - \gamma_0\left[1 - \frac{\theta^2}{\theta_0^2}\right]\frac{d\theta}{dt} + \omega^2\theta = 0 \tag{2.2}$$

Typical trajectories in $(\theta, \dot{\theta})$ space are shown in Fig. 2. In this system, trajectories tend toward a stable periodic orbit or limit cycle, which is an attractor of dimension one.

2.2. *Strange attractors*

For many attractors, the attracting set can be very complicated, and even of non-integer dimension. Sets of non-integer dimension have been termed 'fractal' by Mandelbrot [6], and if they are attractors, they are said to be 'strange'. This definition of a 'strange attractor' refers to its geometrical structure, and may be refined in a more formal way [7].

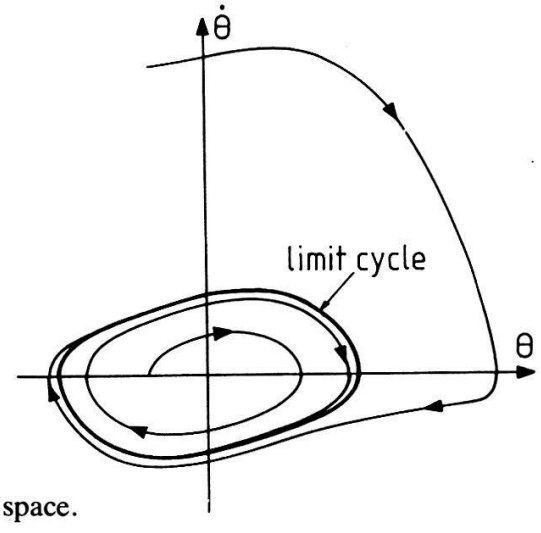

Figure 2
Typical trajectories of the Van der Pol oscillator in $(\theta, \dot{\theta})$ space.

2.3. *Chaotic attractors*

The volume contraction corresponding to a dissipative dynamical system does not necessarily contract lengths in all directions. In some directions they may be stretched, as long as in others they are sufficiently contracted to reduce the initial volume. Trajectories that are arbitrarily close initially may separate with time, even on the attractor. In other words, chaotic motion is characterized by an exponentially growing separation between nearby trajectories. This property is called 'sensitive dependence on initial conditions', and attractors exhibiting this property are termed 'chaotic'. It has to be noted that this dynamical characteristic of the attractor is sometimes included in the definition of strange attractors, though there exist strange attractors that are not chaotic [3, 7].

2.4. *Deterministic chaos*

Physical systems that can be described in terms of differential or difference equations, for which future time behaviour can be calculated from given initial conditions, are called 'deterministic'. It has been shown by Poincaré [8] and Lorenz [9] that chaotic trajectories can be governed by simple sets of non-linear differential or difference equations. In the following, 'deterministic chaos' will be used to denote the irregular or chaotic motion which is generated by non-linear deterministic systems. It should be noted that chaos is not necessarily restricted to dynamical systems with a very large number of degrees of freedom: it can be shown that three degrees of freedom suffice to generate chaotic behaviour [10].

3. Characterization of dynamical systems

It is of interest to know whether there exist criteria by which the chaotic motion of deterministic systems can be distinguished from one another and from random motion. Fourier analysis of an observable (for example) is very often insufficient to provide such a distinction. Therefore, new methods have to be used to characterize these systems [2]. In the following sections, we discuss three important types of measures that are available to provide a useful characterization of chaotic motion.

3.1. *Kolmogorov entropy*

For a chaotic system, trajectories arising from two initial conditions that are different, but indistinguishable within a given defined precision, will become distinguishable after a finite interval of time. Thus, in contrast to regular motion, chaotic trajectories continually reveal new information about the system. The mean rate of 'creation' of information is measured by the Kolmogorov (or metric) entropy K, which provides a means of quantifying the degree to which a dynamical system is chaotic [11]. K is zero for regular motion, infinite for random systems, but is finite and positive for systems exhibiting deterministic chaos. A

more complete description of the Kolmogorov entropy may be found in Refs. [15, 16, 20, 65].

3.2. *Lyapunov exponents*

The spectrum of Lyapunov (or characteristic) exponents [12] quantifies the average stability properties of trajectories on an attractor. These stability properties are determined by the response of the system to small perturbations. A system can be stable to perturbations in some directions, but unstable in others. For a system of dimension d, the spectrum of Lyapunov exponents λ_i, $i = 1, \ldots, d$, provides a dynamical measure of the exponential rate of divergence (or, convergence) of initially nearby trajectories, in d orthogonal directions. Chaotic systems are characterized by the existence of at least one positive Lyapunov exponent, while for regular systems all exponents are negative or zero. A discussion of the calculation of the spectrum of Lyapunov exponents for a chaotic system will be given in Section 6.3.

3.3. *Generalized dimensions*

The generalized dimensions [13], have recently become, due to the existence of simple algorithms, the most common characterization of chaotic dynamical systems. These dimensions provide a static measure of the properties of an attractor.

3.3.1. *The infinite number of generalized dimensions.* Attractors can be characterized by an infinite number of different generalized dimensions D_q, $q > 0$. It has been asserted [14] that a complete knowledge of the set of dimensions D_q is equivalent to a complete physical characterization of the attractor. To date, only three different dimensions have been studied extensively: the Hausdorff dimension D_0, the information dimension D_1 and the correlation dimension D_2.

These generalized dimensions are defined as follows. Consider a strange attractor embedded in an m-dimensional space, and let $\vec{X}_i$, $i = 1, \ldots, N$ be a finite section of a discretized trajectory on the attractor. Cover phase space with a mesh of cells of size r^m and let $M(r)$ be the total number of cells containing points of the series $\vec{X}_i$. The probability p_k of finding a point in the cell k is then given by

$$p_k = \lim_{N \to \infty} \frac{N_k}{N} \tag{3.1}$$

where N_k is the number of points in cell k. The infinite set of generalized dimensions D_q that characterizes the inhomogeneous static structure of the attractor is then defined through the q-th power of p_k as [14, 15]

$$D_q = \frac{1}{(q-1)} \lim_{r \to 0} \frac{\log \left(\sum_{k=1}^{M(r)} p_k^q \right)}{\log r} \tag{3.2}$$

with $q \geqslant 0$, but not necessarily integer.

For $q = 0$, equation (3.2) becomes

$$D_0 = -\lim_{r\to 0} \frac{\log\left(\sum_{k=1}^{M(r)} 1\right)}{\log r} = \lim_{r\to 0} \frac{\log M(r)}{\log r} \tag{3.3}$$

which is the usual definition of the Hausdorff dimension (also denoted by D), sometimes called the similarity or fractal dimension.

For $q \to 1$, equation (3.2) becomes

$$D_1 = \lim_{r\to 0} \frac{\sum_{k=1}^{M(r)} p_k \log p_k}{\log r} = -\lim_{r\to 0} \frac{S(r)}{\log r} \tag{3.4}$$

According to the theory of the measure of information [16], $S(r) = -\sum_{k=1}^{M(r)} p_k \log p_k$ is the minimal information needed to locate a point on the attractor with precision r. S has been called the 'information-theoretic entropy' [17, 18], and therefore D_1 (also denoted by σ) – which is sensitive to the visiting frequency on the attractor – is named the 'information dimension'.

If $q = 2$, equation (3.2) becomes

$$D_2 = \lim_{r\to 0} \frac{\log\left(\sum_{k=1}^{M(r)} p_k^2\right)}{\log r} \tag{3.5}$$

which is the definition of the correlation dimension (also denoted by ν), that will be treated in detail in Section 4.

The three commonly used dimensions are therefore defined as:

$$D \equiv D_{q=0} \tag{3.6}$$

$$\sigma \equiv \lim_{q\to 1} D_q \tag{3.7}$$

$$\nu \equiv D_{q=2} \tag{3.8}$$

Generalized dimensions D_q with other integer q correspond to exponents associated with ternary, quaternary and higher order correlation functions. It has been shown [14] that the D_q are ordered such that $D_q \geqslant D_{q'}$ for any $q' > q$, where the equality sign holds only if the attractor is homogeneous. All generalized dimensions are therefore bounded between D, the Hausdorff dimension, and D_∞. Specifically,

$$\nu \leqslant \sigma \leqslant D \tag{3.9}$$

3.3.2. *Examples of the Hausdorff dimension.* Consider first the Hausdorff dimension of the following sets:

(1) a point $\to M(r) = 1 \quad \to D = 0$

(2) a line of finite length $\to M(r) \sim 1/r \to D = 1$

(3) a surface of finite area $\rightarrow M(r) \sim 1/r^2 \rightarrow D = 2$

In each case, these results correspond to the standard definition of Euclidean dimension.

As an application to a simple set of non-integer dimension, consider the Cantor set, constructed by iteratively ($i = 0, 1, 2, \ldots$) deleting the middle third of each remaining segment of a unit interval (see Fig. 3). In this case,

$$\begin{aligned} &\text{for } i = 0 \quad r = 1 \quad M(r) = 1 \\ &\quad i = 1 \quad r = \tfrac{1}{3} \quad M(r) = 2 \\ &\quad i = 2 \quad r = \tfrac{1}{9} \quad M(r) = 4. \end{aligned}$$

In general, $M(r) = 2^i$, $r = (\frac{1}{3})^i$, and thus $D = \log 2/\log 3 \approx 0.63$. In terms of its dimension, the Cantor set can be viewed as a geometrical object 'between a point and a line'.

3.4. *Relations between measures of chaos*

It has been established that there exist relations between the three measures described in the previous sections.

A knowledge of the spectrum of Lyapunov exponents can provide an upper bound for the Kolmogorov entropy of a chaotic dynamical system. This is obtained through the inequality [13, 19]:

$$K \leqslant \sum_i \lambda_i^+ \tag{3.10}$$

where λ_i^+ are the positive Lyapunov exponents. For the case of equality in equation (3.10), which often seems to hold [2], this relation is called the Pesin identity [20].

A relation between the Lyapunov exponents and the Hausdorff dimension has been suggested by Kaplan and Yorke [21]. They have defined a dimension, which is denoted as D_{KY}, via the Lyapunov exponents:

$$D_{\mathrm{KY}} = j + \frac{\sum_{i=1}^{j} \lambda_i}{|\lambda_{j+1}|} \tag{3.11}$$

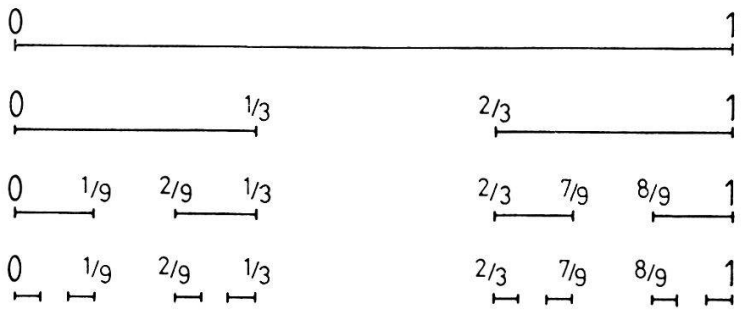

Figure 3

Construction of the Cantor set.

where j is the largest integer for which $\sum_{i=1}^{j} \lambda_i > 0$. (By convention, the exponents are ordered such that $\lambda_1 \geqslant \lambda_2 \geqslant \cdots \geqslant \lambda_d$.) Kaplan and Yorke have conjectured that D_{KY} is equal to the Hausdorff dimension D: this has been shown to hold for many examples that have been considered (see, for example Refs. [13, 22]).

3.5. *Reconstruction of an attractor*

When dealing with experiments (as opposed to computer simulations), it is generally not possible to have access to the m simultaneous signals necessary to describe the trajectory in the m-dimensional phase space. Frequently, in fact, the temporal dependence of only one scalar variable is monitored.

Fortunately, it has been shown to be possible to reconstruct certain properties of an attractor in phase space from the time series of a single variable [23, 24]. The principle behind the reconstruction method is to create a set of m-dimensional vectors from a single time series $x_i = x(t_i)$, $i = 1, N_s$, with the x_i corresponding to measurements regularly spaced in time. This process is termed 'embedding' and m is called the 'embedding dimension'.

One possible method is to take $(m-1)$ successive derivatives $x(t)$, $\dot{x}(t)$, $\ddot{x}(t), \ldots$ of $x(t)$. Unfortunately, this procedure amplifies numerical errors. A preferable method is to introduce a time lag p such that the m-dimensional vectors have the form

$$\vec{X}_i = [x(t_i), x(t_i + p), \ldots, x(t_i + (m-1)p)] \tag{3.12}$$

In principle, all three measures introduced in Sections 3.1.–3.3. – namely the Kolmogorov entropy, the Lyapunov exponents and the generalized dimensions – are accessible through this reconstruction (J. P. Eckmann 1986, private communication). Nevertheless, it should be noted that in practice, the construction of phase-space coordinates may not always be straightforward. This is because there is no *a priori* knowledge of the most appropriate choice of parameters to be used in the reconstruction of an attractor. Guidelines to assist in the choice of parameters will be given in Section 4.2.

3.6. *Comments on available algorithms*

Two different types of data will be analysed in this paper, namely those generated numerically and those from experiments involving real physical systems. When dealing with the equations of a dynamical system, it is possible to solve the evolution equations with an accuracy limited only by the precision of the computer. Real physical experiments, however, yield data containing only a restricted amount of information. This is due to the presence of noise, the generally poor dynamical range of data acquisition systems and the fact that the desired observables are not necessarily measurable. This basic difference may restrict the application of algorithms which calculate the 'measures of chaos' for experimental data. (For a more detailed survey of these problems, see Ref. [2].)

There have been several attempts to develop algorithms for the calculation of the Kolmogorov entropy that may be applied even to experimental data [25, 27]. However, these algorithms tend not to be robust, and therefore are very seldom used to characterize signals from real physical systems.

The evaluation of the spectrum of Lyapunov exponents is based on the study of the evolution of small perturbations of the physical system. An algorithm that can be applied when the equations of motion governing the system are known, is described in Section 6.3. For the case when the equations of motion are not known, e.g. for experimental data, algorithms have recently been proposed by several authors [28–31]. However, these algorithms require a great deal of care in their application, even for numerically generated data.

The measurement of dimensions is the most straightforward method applicable to experimental data. The Hausdorff and information dimensions, in principle, may be calculated using the 'box-counting' algorithms introduced in Section 3.3. Despite some improvements [32], such algorithms converge very slowly even for low-dimensional attractors ($D < 2$), and do not converge for higher dimensional attractors ($D > 2$) [33]. However, the correlation dimension has been shown to be accessible through recently developed algorithms [18, 34, 66]. These algorithms have been found to be sufficiently robust to be applied to experimental data, and have consequently been extensively used in recent years. Nevertheless, it should be stressed that in any given experiment, one deals with discretized time series of finite resolution and finite length. Natural limits therefore exist on the applicability of these algorithms. In the next section, a detailed discussion on the application of the Grassberger–Procaccia algorithm is presented.

4. The correlation dimension

4.1 *The Grassberger–Procaccia algorithm*

The algorithm developed by Grassberger and Procaccia for the calculation of the correlation dimension ν makes use of equation (3.5) with the following evaluation:

$$\sum_{k=1}^{M(r)} p_k^2 \equiv \text{probability that a cell } r^m \text{ contains two points of the attractor}$$

$$\simeq \text{probability that the distance between those two points in less than } r$$

$$= \lim_{N\to\infty} \frac{1}{N^2} \{\text{no. of pairs } i, j \text{ such that } |\vec{X}_i - \vec{X}_j| < r\}$$

$$\equiv C(r)$$

The correlation integral $C(r)$ is defined by

$$C(r) = \lim_{N\to\infty} \frac{1}{N^2} \sum_{i=1}^{N} \sum_{j\neq i=1}^{N} \theta(r - |\vec{X}_i - \vec{X}_j|) \tag{4.1}$$

where N is the number of m-dimensional vectors and θ is the Heaviside step function.

The correlation dimension is then given by

$$\nu = \lim_{r\to 0} \frac{\log C(r)}{\log r} \tag{4.2}$$

The algorithm therefore consists of counting the fraction of points of the attractor contained in an m-dimensional hypersphere of radius r, averaged over the attractor. A finite value of ν indicates that this fraction is proportional to r^{ν} for small r. A direct analogy to the volume of hyperspheres of integer dimension can be drawn.

4.2. *Algorithm application to a single time series*

In practice, the correlation integral $C(r)$ is plotted as a function of r on a log–log graph for a range of values of the embedding dimension m. The slope of the curves is called the correlation dimension ν, if it converges for small r and for a range of m values. The algorithm parameters have to be chosen carefully to provide an appropriate reconstruction of the attractor.

4.2.1. *The embedding dimension m.* The correlation integral cannot increase faster than r^m for a given choice of embedding dimension m. As a result, the slope of $\log C(r)$ vs $\log r$ curves will converge (if at all) to m rather than ν, for $m < \nu$. An adequate choice of the embedding dimension is $m \geqslant \nu$, and may even be $m \geqslant 2\nu + 1$ [2, 24, 35]. If a value of m is chosen that is too large, convergence problems result from poor statistics [34]. This difficulty arises because the number of m-dimensional vectors that can be formed from a given set of data is too small. Since ν is normally not known beforehand, the most effective choice of m has to be determined by trial and error. Typically, this is done systematically by scanning m from small to large values and noticing the m value where the slopes no longer increase with increasing m.

4.2.2. *The meaningful range of r.* The range of r, and therefore $C(r)$ values over which the slope described above can be measured is restricted. For large r, nearly all the points on the attractor are correlated – in other words each hypersphere of radius r contains almost the entire attractor – and $C(r)$ tends towards one. On the other hand, since the number of data points is limited, the statistics for small r are poor and a large scatter in the values of $C(r)$ results. Therefore, there is only a restricted 'meaningful range of r' in which the distribution of distances between pairs of points is statistically useful [2].

4.2.3. *The time delay p.* For proper reconstruction of the attractor from a time series, the time delay p must also be chosen within certain bounds. If it is too small, $x(t_i) \simeq x(t_i + p) \simeq \cdots \simeq x(t_i + (m-1)p)$, resulting in a strong compression in the reconstructed attractor.

On the other hand, p should not be taken too large since distant values in the same vector $\vec{X}_i$ are uncorrelated, leading to a filling of the complete m-dimensional phase space [34].

This indicates that p should be chosen to be less than τ, but greater than τ/m, where τ denotes the 'characteristic time' for the signal $x(t)$. Here, τ is defined as the quarter-period for pseudo-periodic signals, or the e-folding time of the auto-correlation function for broadband chaotic signals.

4.2.4. *Number of points N_s and sampling interval t_s.* In practice, the N_s data points are acquired at a sampling interval t_s. These parameters should be chosen so as to yield sufficient resolution over the desired frequency range of the Fourier spectrum of $x(t)$. In addition, N_s must be large enough for the calculated values of $C(r)$ to be statistically adequate, especially for attractors of large dimension. This may, for the investigation of experimental data, involve some compromise since the parameters of the system should remain constant (to avoid transients) during the total time $N_s \cdot t_s$ for which data are recorded.

4.2.5. *Avoiding spurious correlations.* Calculation of the correlation integral as defined in equation (4.1) may not lead to a reliable determination of the correlation dimension if the value of N_s is too restricted. For certain values of r, the value of $C(r)$ may be overestimated, especially for large values of embedding dimension m. As a result, there may not exist a sufficiently large range of r over which $C(r)$ scales like r^{ν} or, alternatively, a false value of the correlation dimension may be deduced.

The origin of this overestimation has been shown [36] to be the correlations that arise when vectors $\vec{X}_i$ and $\vec{X}_j$ are considered, even though the time difference $|t_i - t_j|$ is not large compared to the characteristic time.

If the total number of data points N_s is too limited, the correlation integral will be dominated by these 'spurious' correlations. In other words, the spatial structure of the attractor will be poorly represented due to the highly non-uniform visiting of different regions of the attractor. This problem is more acute when large embedding dimensions are considered due to the need for a larger number of points to represent correctly the structure of the attractor.

In principle, these spurious correlations can be avoided by choosing N_s sufficiently large. However, in practice, this may not always be easily achieved. It is usually more straightforward simply to avoid counting those pairs of vectors that are close in time, by using a generalization of equation (4.1) [36]:

$$C_k(r) = \lim_{N\to\infty} \frac{2}{N^2} \sum_{i=1}^{N-k} \sum_{j=i+k}^{N} \theta(r - |\vec{X}_i - \vec{X}_j|) \tag{4.3}$$

Note that setting $k = 1$ recovers the standard formulation of equation (4.1), that is, $C_1(r) \equiv C(r)$. In general, k should be chosen such that $k \cdot t_s > \tau$, the values of $C_k(r)$ saturating for k sufficiently large. This requirement is not too restrictive, since it is still possible to satisfy $k \ll N$. Thus for correctly sampled and treated time series data, the above modification is minor in terms of the total number of pairs of vectors considered.

4.3. *Implementation of the algorithm*

All the experimental data analysed in this paper have been acquired using Lecroy TR 8837 Camac analog-to-digital converters, yielding records of 8 bit resolution and $N_s = 8192$. To be consistent with the experimental cases, most studies undertaken using mathematically generated data had the same acquisition parameters.

The resolution in the correlation integral is given by the reciprocal of the total number of distances $|\vec{X}_i - \vec{X}_j|$ that are computed. To optimize this resolution, and therefore to determine more accurately the values of $C_k(r)$ for small values of r, the correlation integral for a given data record was generally calculated using the maximum number of points available. For an embedding dimension m and time delay p, this enables $N = N_s - (m-1) \cdot p \cdot t_s^{-1}$ vectors to be constructed. The total number of distances computed for the calculation of the modified correlation integral $C_k(r)$ is $(N-k+1)(N-k)/2$. For typical values of $N_s = 8192$, $m = 10$ and $p = 4t_s$, this amount to 3.3256×10^7 distances for $k = 1$ and 3.3182×10^7 for $k = 10$. As indicated in the previous section, only a very slight decrease in the total number of distances computed results therefore from the modification of the correlation integral.

In order to calculate the correlation integral for such a large number of vectors, an efficient numerical method is required.[2]) Although any suitable norm can be used to compute $|\vec{X}_i - \vec{X}_j|$, we have chosen the Euclidean norm for our analysis. Programs to calculate $C_k(r)$ over the meaningful range of r, for specified values of p and k and several values of m, have been written for three computer systems that are available to us, i.e., PDP 11/60, CYBER 855 and CRAY 1S-2000. All programs were written in standard FORTRAN, and optimized for each system. Use was made of the shifting and masking procedures available in FORTRAN on each of the three compilers, to bin efficiently the computed distances into geometric order [34]. Special attention was paid to vectorization of the program used on the CRAY 1S-2000. Computation time for a standard case with $N_s = 8192$, $p = 4t_s$, $k = 1$, $m = 2 \rightarrow 10$ and 70 values of r was 34,000 sec (single-user real time) for the PDP 11/60, 5000 CPU sec for the CYBER 855, and 300 CPU sec for the CRAY 1S-2000.

---

[2]) Some authors [37, 38] have reduced the computation time by summing over a small number (≈ 100) of randomly chosen values of the index j. This is suggested not to affect the computed values of $C(r)$. The resolution in $C(r)$ is, however, still given by the total number of distances computed: we have therefore preferred to maximize the number of computed distances by summing over all values of indices i and $j < i$.

5. Application of the Grassberger–Procaccia algorithm

5.1. *Tests on known mathematical attractors*

To test the implementation of the algorithm described above, time series from mathematical systems with known attractors have been analysed. The systems, all of which display chaotic behaviour, are discussed in order of increasing dimension.

5.1.1. *Two-dimensional maps.* As a specific example, the Hénon map [39] has been examined:

$$x_{n+1} = y_n + 1 - ax_n^2$$
$$y_{n+1} = bx_n \tag{5.1}$$

with $a = 1.4$, $b = 0.3$

Figure 4(a) shows the result of plotting 10^4 successive points obtained by iterating equation (5.1) from starting point $x_0 = 0$, $y_0 = 0$. It can be verified that

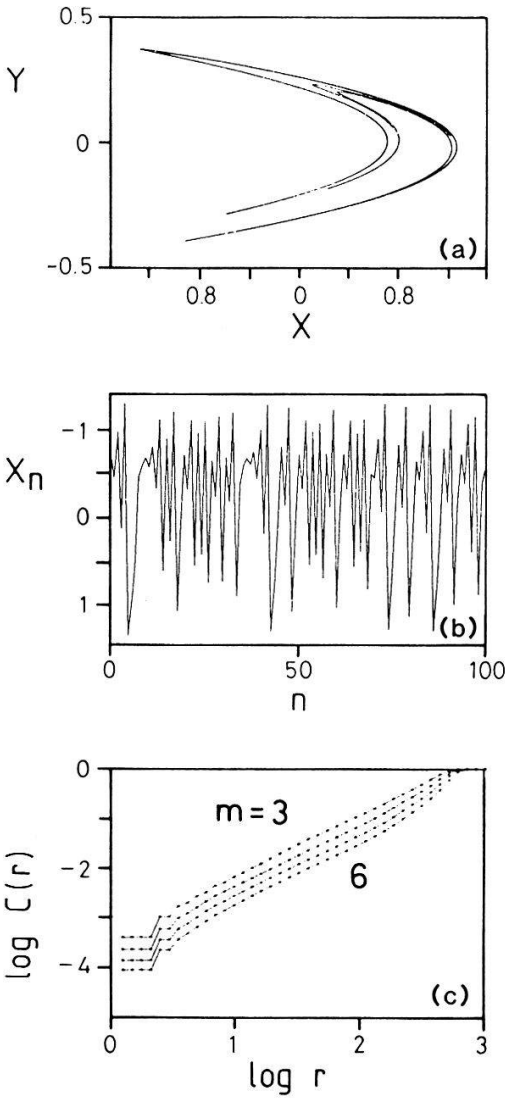

Figure 4
(a) The Hénon map; (b) 100 points of the x-coordinate displayed as X_n vs n (for clarity, the points have been joined by straight line segments); (c) plot of the correlation integral, yielding $\nu = 1.25 \pm 0.1$.

initially close points diverge exponentially [40]. For the correlation analysis, 8192 successive points of the x-coordinate have been acquired after the 1000th iteration. Figure 4(b) displays the first 100 points of the record, joined by straight line segments, in a x_n vs n plot that highlights the chaotic behaviour of the system. Figure 4(c) shows the corresponding logarithmic plots of $C(r)$ vs r, for four consecutive values of m. (All logarithm plots in this paper are calculated using base 10.) It can be seen that for increasing m, the slope of the $C(r)$ vs r converges, and yields a value of $\nu = 1.25 \pm 0.1$. This result should be compared with the values found in the literature: $D = 1.26$ [22] and $\nu = 1.25 \pm 0.02$ (obtained by analysing the attractor without reconstruction, using $N = 20{,}000$) [18].

We have undertaken a similar study for the Kaplan–Yorke map [21] (see Table I).

5.1.2. *Systems of first order differential equations.* As an example of such a system, the Lorenz model [9] has been studied:

$$\begin{aligned} \dot{x} &= \sigma(y - x) \\ \dot{y} &= -y - xz + Rx \\ \dot{z} &= xy - bz \end{aligned} \tag{5.2}$$

with $R = 28$, $\sigma = 10$, $b = \frac{8}{3}$.

These three coupled non-linear equations have been integrated numerically using a standard Runge–Kutta method, with adjustment of the integration time step to provide the desired precision. After a time interval $\Delta t = 10$, 8192 vectors (x, y, z) separated by time intervals $t_s = 0.1$ were recorded (see Figs. 5(a), (b)). The z-coordinate was used for the present analysis. The characteristic time for this record was calculated to be $\tau \simeq 0.4$. For the calculation of the correlation integral, a time delay of $p = 0.4$ was therefore used. The resulting logarithmic plot of $C(r)$ versus r, shown in Fig. 5(c), exhibits a saturation in slope yielding a value of $\nu = 2.16 \pm 0.3$. This result should be compared with the tabulated values of $D = 2.06 \pm 0.01$ [22] and $\nu = 2.05 \pm 0.01$ (using $N = 15{,}000$) [18].

5.1.3. *Summary of the results.* The values of the correlation dimension that have been found for the analysed mathematical systems are listed in Table I.

Taking into account the smaller number of points ($N_s = 8192$) and the limited (8 bit) resolution, the agreement between correlation dimensions is very good.

Table I
Comparison of the calculated values of the correlation dimension of known mathematical attractors, with dimension values given in the literature.

Attractor	$\nu_{[18]}$	N	$D_{[22]}$	$\nu_{\text{calculated}}$
Hénon	1.25 ± 0.02	20,000	1.26	1.25 ± 0.1
Kaplan–Yorke	1.42 ± 0.02	15,000	1.431	1.4 ± 0.25
Lorenz	2.05 ± 0.01	15,000	2.06 ± 0.01	2.16 ± 0.3

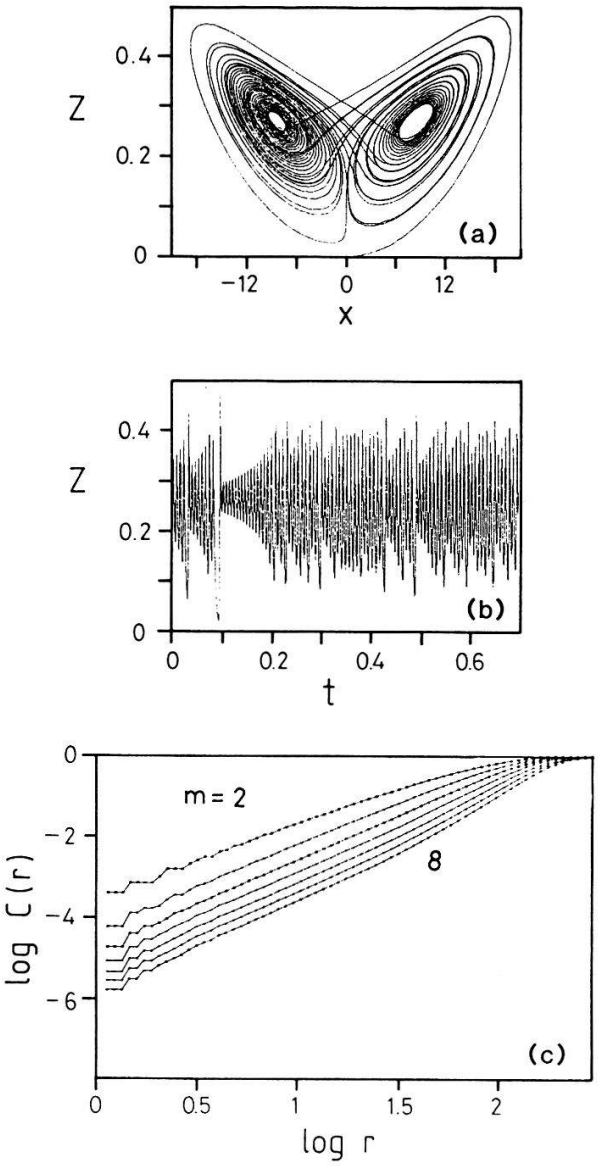

Figure 5
(a) The Lorenz attractor; (b) time behaviour of the z-coordinate; (c) plot of the correlation integral, yielding $\nu = 2.16 \pm 0.3$.

This provides confidence in our application of the algorithm to more complex, and less studied, chaotic systems.

5.2. *Separation of noise from deterministic chaos*

Before applying the correlation algorithm to real data, the practical question has to be raised as to whether ν can be accurately determined from experimental data, for which noise can be expected to smear the fractal structure of the strange attractor.

Random noise can be considered to be the result of the superposition of a very large number of independent oscillating modes. Therefore, if a noise signal is analysed using the algorithm, it should have a very large dimension and $C(r)$ should always scale like r^m (see Fig. 6).

In the case of low amplitude noise superimposed on a deterministic signal, the existence of noise will not destroy the fractal structure, but will cause

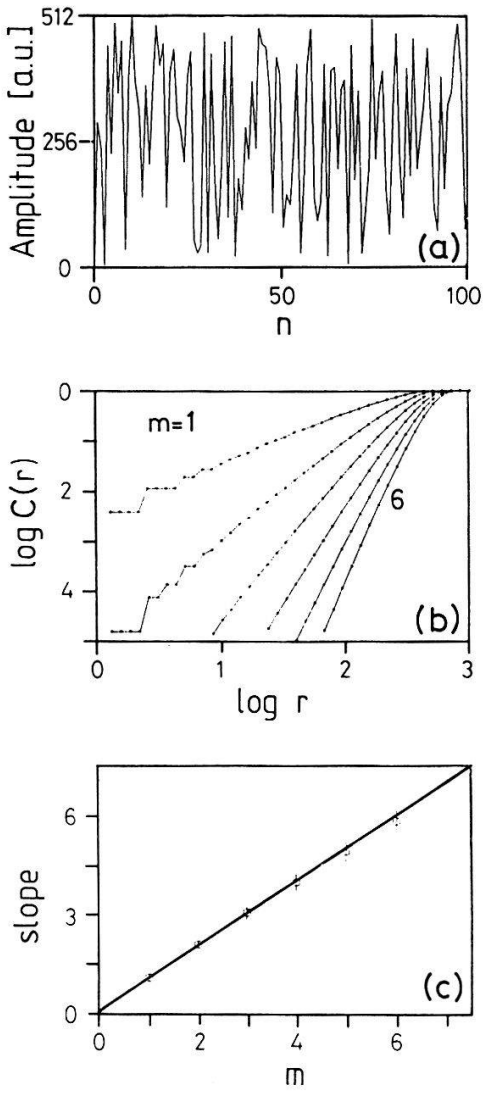

Figure 6
(a) Random noise signal, with (b) the corresponding plot of the correlation integral, and (c) the slope of the $C(r)$ vs r curves as a function of embedding dimension m.

fuzziness on length scales that are smaller or equal to the noise amplitude [41]. In other words,

$$C(r) \propto r^m \quad \text{for} \quad r \leqslant r_{\text{noise}}$$
$$C(r) \propto r^\nu \quad \text{for} \quad r \geqslant r_{\text{noise}} \tag{5.7}$$

Figure 7 shows the example of the Hénon map x-component with added random noise (signal-to-noise ratio = 4.2%). Both 'length' scales can be identified, namely the total data amplitude of 490 [a.u.], as well as the noise amplitude of 20 [a.u.] indicated by the inflexion of the $C(r)$ vs r curves. Therefore, the correlation algorithm not only provides a tool to differentiate between random noise and deterministic chaos, but may also supply information on the noise level of the system.

5.3. *The effect of data filtering*

Any measurement of experimental signals is, to some extent, filtered due to finite instrumental bandwidth. Often data are additionally filtered to remove

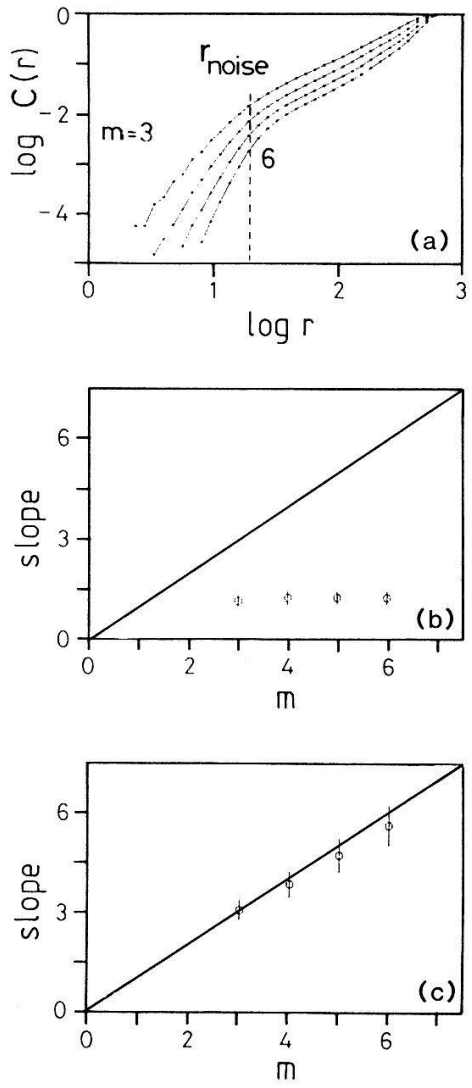

Figure 7
Correlation analysis of the x-coordinate of the Hénon map with superimposed random noise. In (a) the correlation integral is shown, with the corresponding slopes of the curves plotted in (b) at $r = 100$ and (c) at $r = 7$.

noise and/or to satisfy the Nyquist acquisition frequency criterion. For the interpretation of correlation dimensions obtained from experimental data, it is therefore of crucial importance to know and, if possible, to quantify the effect of filtering.

It appears intuitive that filtering may reduce the dimension of a signal by removing information. However, it has recently been shown [42] that an increase of dimension may result. This conclusion was reached by considering the simple example of a single-pole low-pass filter, but might still be valid for more complicated multi-pole filters. Further studies are necessary to elucidate the effect of data filtering.

6. The bipolar motor: theoretical study

A dipole magnet placed in a linearly polarized, oscillating magnetic field forms a dynamical system exhibiting both periodic and chaotic motions. It may therefore serve as a simple mathematical model for analysing the behaviour and techniques described in the previous sections.

In this section, the motion of a bipolar motor is mathematically described by the solutions of a set of non-linear differential equations. The dependence of the character of the motion, as a function of the amplitude of the driving field is illustrated. It is shown that this system follows a period-doubling route to chaos. The spectrum of Lyapunov exponents is calculated, and their usefulness in characterizing the chaotic motion of a bipolar motor is demonstrated.

The mathematical model of the bipolar motor is also used to support statements made in Section 5. The reconstruction of an attractor using delay coordinates is illustrated, demonstrating the consequences of good, and inappropriate, choices of the parameters used in the reconstruction. The application of the algorithm for calculation of the correlation dimension is also studied.

6.1. *Equation of motion*

The equation of motion for a dipole magnet in a linearly polarized magnetic field oscillating at frequency ω is

$$\ddot{\theta} + \gamma\dot{\theta} + f \sin\theta \cos\omega t = 0 \tag{6.1}$$

Here, we have assumed that the damping force is proportional to the angular velocity $\dot{\theta}$ of the magnet, with a damping coefficient γ. The static coefficient of damping is thus assumed to be zero. The amplitude of the driving force is $f = \mu B_\omega / I$, where μ and I are, respectively, the magnetic moment and moment of inertia of the magnet, and B_ω is the amplitude of the oscillating magnetic field. Equation (6.1) can be written in terms of three autonomous first order differential equations:

$$\begin{aligned} \dot{\theta} &= \Omega \\ \dot{\Omega} &= -\Gamma \cdot \Omega - F \cdot \sin\theta \cdot \cos t \\ \dot{t} &= 1 \end{aligned} \tag{6.2}$$

where $\Gamma = \gamma/\omega$ and $F = f/\omega^2$.

6.2. *Numerical solutions*

The three coupled equations (6.2) have been integrated, as was the Lorenz system discussed in Section 5.1.2, using a standard Runge–Kutta method. Three typical solutions are shown in Fig. 8. These solutions were obtained using a value of $\Gamma = 0.4$ and initial conditions: $\theta = 0$, $\Omega = 1$ and $t = 0$. The solutions displayed in Figs. 8(a) and 8(b) for $F = 1.5$ and 2.0, show that after an initial transient phase, the behaviour of the magnet settles into a rotational motion, with a superimposed higher frequency oscillation. For Fig. 8(a), the period of the high frequency oscillation is half the period of the driving force, i.e. $\Delta t = \pi$. The solution shown in Fig. 8(b) has a period of twice that of Fig. 8(a). The solution displayed in Fig. 8(c) for $F = 2.5$, exhibits non-periodic behaviour throughout the time interval shown. Integration over much longer time intervals has indicated

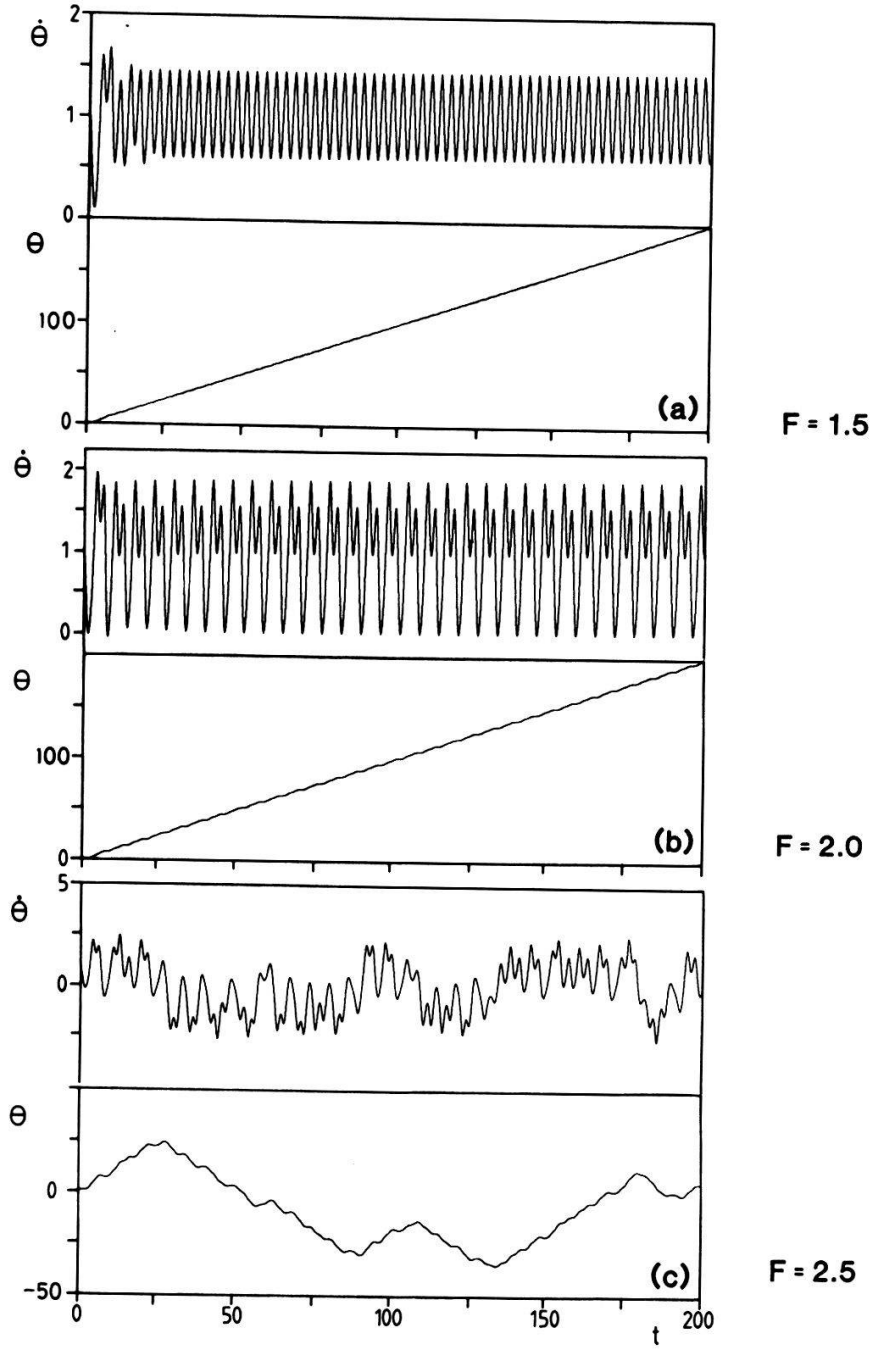

Figure 8
Three typical solutions of the equation of motion of the bipolar motor, for $\Gamma = 0.4$ and (a) $F = 1.5$, (b) $F = 2.0$ and (c) $F = 2.5$.

that the motion of the magnet for this choice of parameters remains chaotic, with no tendency toward periodicity.

These three different types of behaviour exhibited by the bipolar motor can be displayed in several alternative fashions. Figure 9 shows the Fourier spectrum of $\Omega(t)$ for each of the three values of F. The chaotic motion is characterized by a broad spectrum and, correspondingly, a rapidly decaying auto-correlation function.

Another instructive method of displaying the motion of the magnet is via a Poincaré section [5, 15] of the three dimensional space (θ, Ω, t). This is

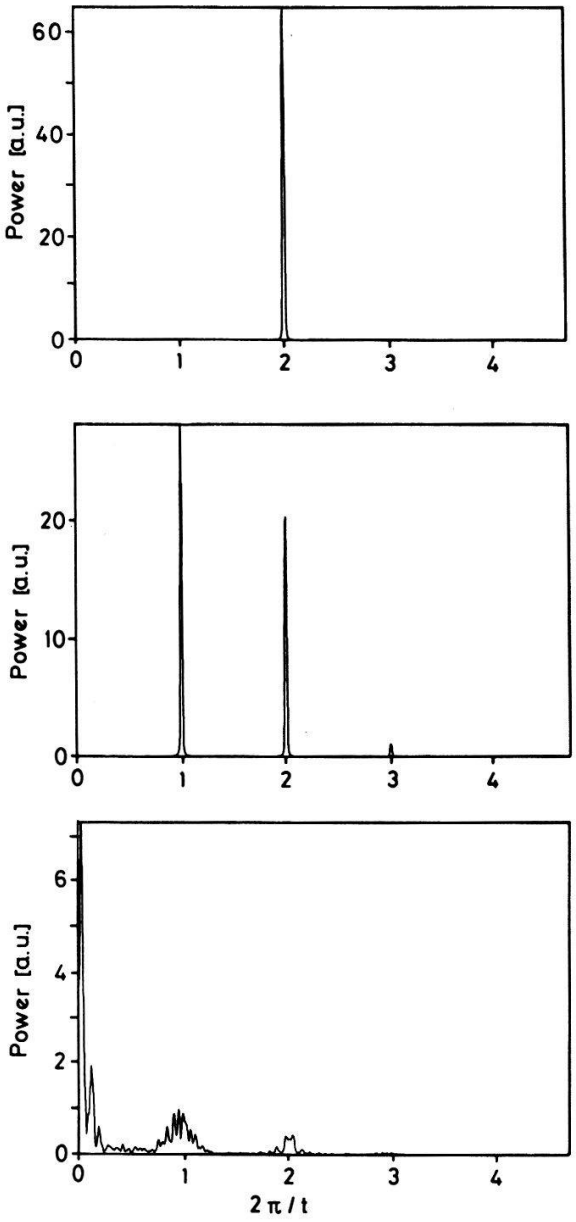

Figure 9
Fourier spectra of the three time signals shown in Fig. 8.

constructed by plotting $(\theta[\mathrm{mod}\, 2\pi], \Omega)$ each period of the driving force, $\Delta t = 2\pi n$ for integer n, after the decay of transients. In such a representation, periodic motion at the same frequency as the driving force is exhibited as a single point and period-doubled motion as two points. More complex motion, in particular chaotic behaviour, results in a more intricate Poincaré plot. Figure 10 shows the Poincaré plot corresponding to $F = 2.5$. This plot demonstrates that even though the temporal behaviour of motion appears chaotic (Fig. 8(c)), the corresponding Poincaré plot exhibits a regular pattern. This representation for chaotic motion thus yields a convenient means of viewing the attractor associated with the motion after the decay of transients. The Poincaré plot shown in Fig. 10 displays the characteristic 'stretching' and 'folding' of phase space associated with strange attractors [15].

6.3. *Lyapunov exponents*

An analysis of the temporal dependence of the solution of equation (6.2), for given values of the parameters Γ and F, yields information about the behaviour of

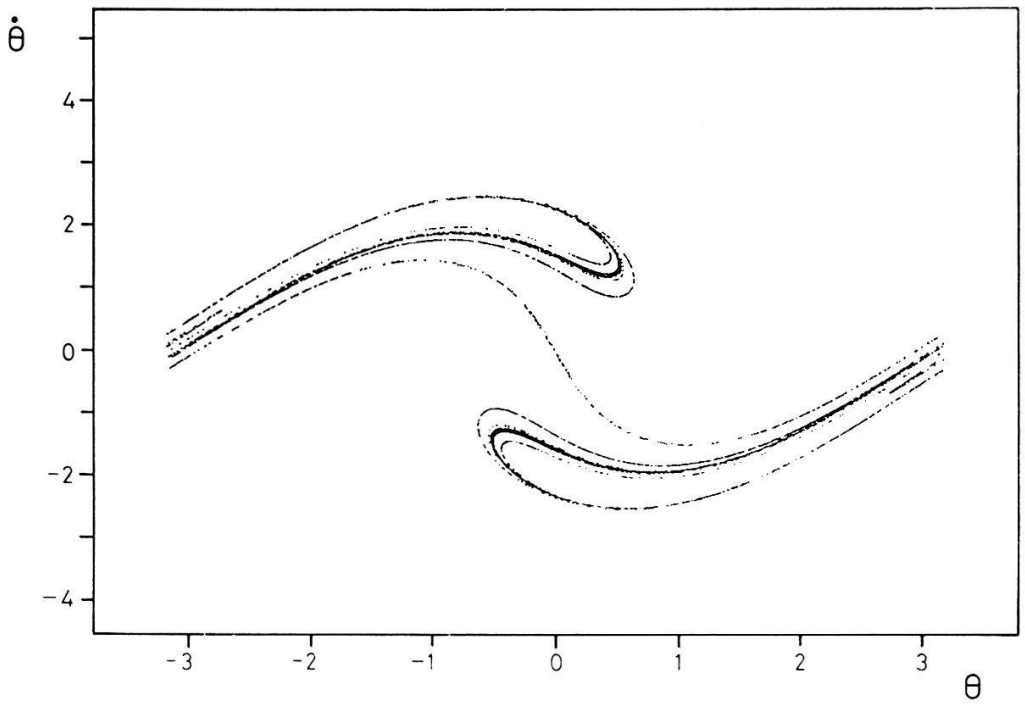

Figure 10
Poincaré plot corresponding to the case $\Gamma = 0.4$, $F = 2.5$, shown in Figs. 8(c) and 9(c). To avoid transients, the points plotted correspond to the 6000 cycles following the first 50 cycles of the driving force.

the bipolar motor. For a more detailed investigation of how the character of the motion depends on the choice of parameters, the representations discussed in the previous section are rather inconvenient. A more straightforward means of distinguishing between periodic and chaotic motions may be obtained through the spectrum of Lyapunov exponents.

In general, if the non-linear equations of motion governing the system are known, the Lyapunov exponents may be calculated by linearizing the equations and studying the evolution of small perturbations over long time intervals. For a set of autonomous equations of order d, consideration of d orthogonal perturbation vectors enables the calculation of the spectrum of Lyapunov exponents, $\lambda_1 \geqslant \lambda_2 \geqslant \cdots \geqslant \lambda_d$.

For the bipolar motor, the spectrum of Lyapunov exponents has been calculated from the equations of motion (6.2). These equations may be written in the form:

$$\dot{\vec{X}} = \vec{J}(\vec{X}), \tag{6.3}$$

where $\vec{X} = (\theta, \Omega, t)$. The evolution of perturbation vectors $\vec{\xi}_i$ in the tangent space at $\vec{X}(t)$ is governed by the first variational equations:

$$\dot{\vec{\xi}}_i = \overleftrightarrow{T}(\vec{X}(t))\vec{\xi}_i, \tag{6.4}$$

where $\overleftrightarrow{T}$ is the Jacobian matrix of $\vec{J}$:

$$\overleftrightarrow{T} = \frac{\partial \vec{J}}{\partial \vec{X}} = \begin{pmatrix} F \cdot \cos \overset{0}{\theta} \cdot \cos t & -\overset{1}{\Gamma} & -F \cdot \sin \overset{0}{\theta} \cdot \sin t \end{pmatrix} \tag{6.5}$$

The mean exponential growth (decay) of the perturbation vector $\vec{\xi}_i$ yields the Lyapunov exponent

$$\lambda_i = \lim_{t\to\infty} \frac{1}{t} \log \left\{ \frac{|\vec{\xi}_i(t)|}{|\vec{\xi}_i(0)|} \right\}. \tag{6.6}$$

Integration of equation (6.4) over long times leads to a divergence of the magnitudes of the perturbation vectors and an inability to distinguish between their directions, in the presence of a direction of rapid growth. To avoid these problems, the perturbation vectors are periodically re-orthonormalized by the Gram–Schmidt procedure [43]. This allows one vector to seek the direction of most rapid local growth (corresponding to λ_1), the second vector to seek the second most rapidly growing direction (corresponding to λ_2), and so on.

For the present calculations, equation (6.3) was first integrated over a time interval $\Delta t = 5000$ (i.e. 796 cycles of the driving force) to avoid transient behaviour that occurs particularly in the sensitive regions of transition between periodic and chaotic motion. The evolution of the vectors $\vec{\xi}_i$ was then determined over the following time interval $\Delta t = 5000$. This proved to be a sufficiently long time interval to ensure convergence of the Lyapunov exponents derived from equation (6.6). The exponents thus determined were found to be independent of the choice of $\vec{X}(0)$ and $\vec{\xi}_i(0)$ as is expected.

Two features of the present system prove of benefit in the calculation of the Lyapunov exponents. Firstly, since the trace of the Jacobian matrix in equation (6.5) is constant, it follows [43] that

$$\sum_{i=1}^{3} \lambda_i = \mathrm{Tr}\,(\overleftrightarrow{T}) = -\Gamma \tag{6.7}$$

Secondly it has been shown [44, 45] that at least one of the Lyapunov exponents vanishes, unless the orbit $\vec{X}(t)$ ends on a fixed point. These two features provide checks on the calculated exponents, or alternatively, allow the spectrum of Lyapunov exponents to be determined from the knowledge of only one non-zero exponent. Our calculations showed that the two methods produced the same results. Therefore, in order to minimize computational time, only the largest exponent was generally calculated using equation (6.6).

Figure 11 shows the dependence of the three Lyapunov exponents calculated for $\Gamma = 0.4$, varying F by steps of 0.05 within the range $1.0 \leqslant F \leqslant 87.0$. This figure shows the presence of bands of chaos (i.e., where $\lambda_1 > 0$) separated by regions of periodic solutions. Within each of the six major bands of chaos shown in Fig. 11 are numerous small regions of periodic solutions: the number of these regions apparent in Fig. 11 is limited by the resolution in F.

A detailed study of the onset of chaos that occurs at the beginning of each major band has revealed a period-doubling route to chaos. Preceding each band occurs a number of values of F for which $\lambda_1 = \lambda_2 = 0$, which we denote by F_n^m for the nth values of the mth band. The beginning of the first band is shown more clearly in the expanded view plotted in Fig. 12. (It is instructive to compare this

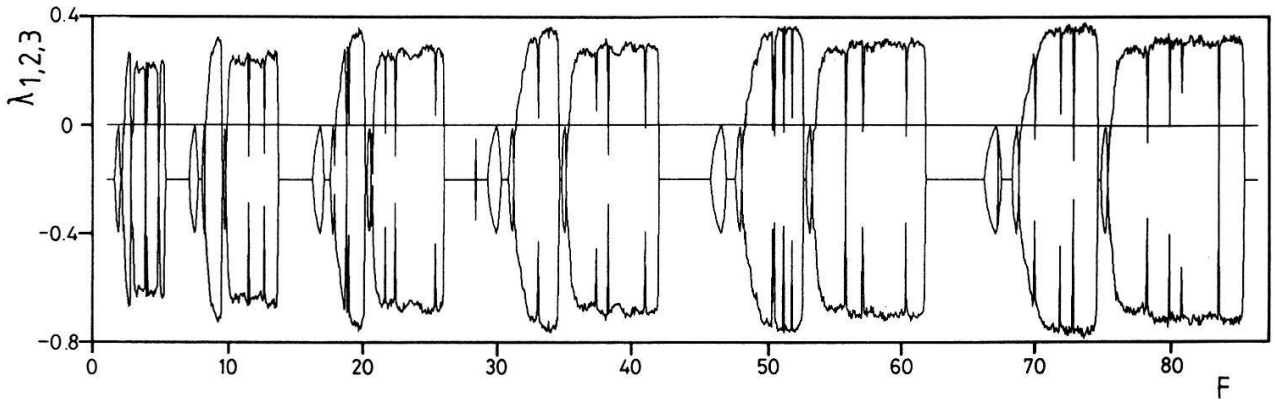

Figure 11
Spectrum of the Lyapunov exponents for the bipolar motor, with $\Gamma = 0.4$ and $1.0 \leq F \leq 87.0$.

diagram with Fig. 3 of [46] for the Rössler system [47] which also exhibits a period doubling route to chaos.) Comparing Figs. 8 and 12 it can be seen that the value of F chosen for Fig. 8(a), $1.5 < F_1^1$, is before period doubling; is after one period doubling for Fig. 8(b), with $F_1^1 < 2.0 < F_2^1$; and is after the transition to chaos for Fig. 8(c), with $2.5 > F_\infty^1$. An analysis of the relationship between different values of F_n^1 is given in the Appendix. It is interesting to note that Fig. 11 shows that $F_1^m \propto m^2$.

It can be seen from Fig. 8(a) that in the periodic region preceeding F_1^1 the system exhibits rotative motion, with superimposed oscillations at twice the driving frequency. This is the usual region of operation of a bipolar motor. In the periodic region preceeding F_1^2, however, the superimposed oscillations have the same frequency as the driving force. The resultant motion of the system is then one of vibration. In fact, it can be shown that in the periodic region preceeding F_1^m, the motion is rotation if m is odd and vibration if m is even. This point is illustrated in Fig. 13. Note that the average angular velocity of rotation is constant ($= 1$), and is not greater for larger values of F for which rotation occurs.

Using the Kaplan–Yorke conjecture, the Hausdorff dimension D_{KY} may be calculated from the spectrum of Lyapunov exponents using equation (3.12). The

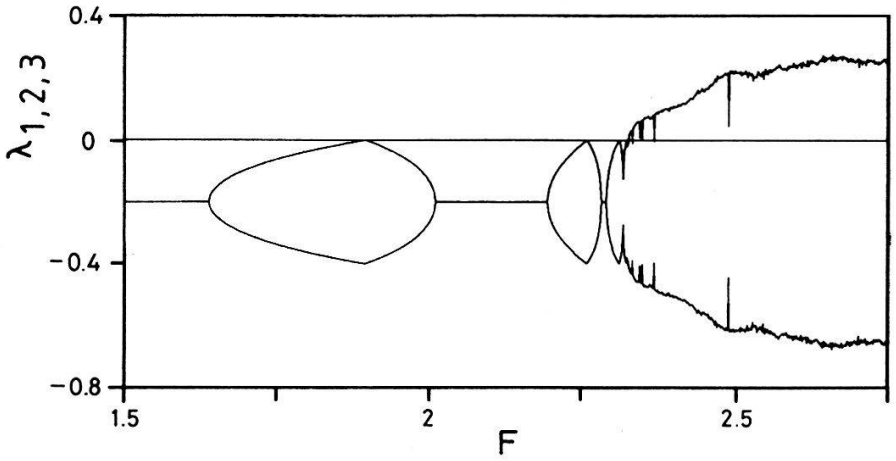

Figure 12
Expanded view of the beginning of the first band of chaos in Fig. 11.

dependence of D_{KY} on the amplitude of the driving force is shown in Fig. 14. For chaotic motion, $2 < D_{KY} < 3$, while for periodic motion $D_{KY} = 1$.

6.4. *Reconstruction of the attractor*

For the mathematical system described by equation (6.2), it is possible to have access to the three-dimensional vector that describes the state of the system at any time. It is therefore straightforward, for given values of Γ and F, to construct a Poincaré plot of the attractor, as shown in Fig. 10. Time series data obtained from numerical integration of equation (6.2) may, however, also be used to elucidate some of the salient features in the reconstruction of the attractor from a single time series, as described in Section 4.

For these studies the time series $\theta(t)$ was used. Parameter values $\Gamma = 0.4$ and $F = 2.5$ were chosen, for which the motion of the system is chaotic. The characteristic time for this time series was calculated to be $\tau = 1.5$. Reconstructed Poincaré plots of the attractor were obtained by plotting $(\theta(t), \theta(t+p))$ each period of the driving force, for various values of the time delay p. Three

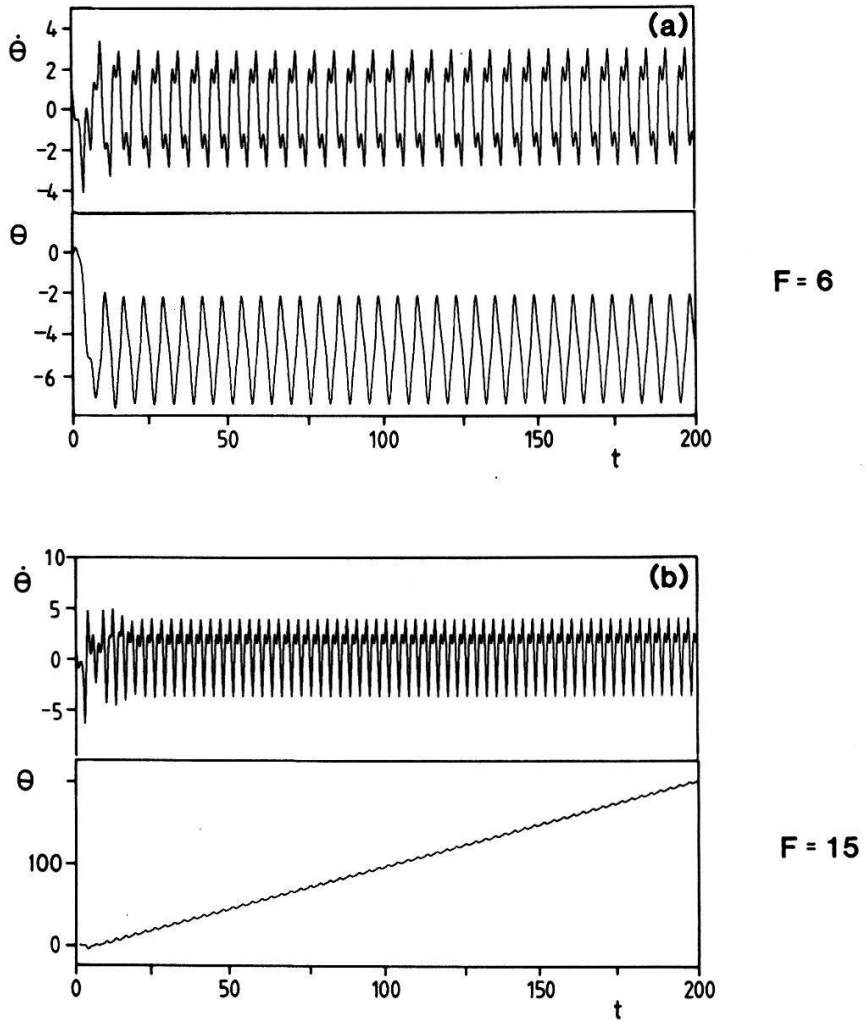

Figure 13
Four periodic solutions of the equation of motion of the bipolar motor, for $\Gamma = 0.4$ and (a) $F = 6$, (b) $F = 15$, (c) $F = 28$ and (d) $F = 44$, showing rotational and vibrational behaviour.

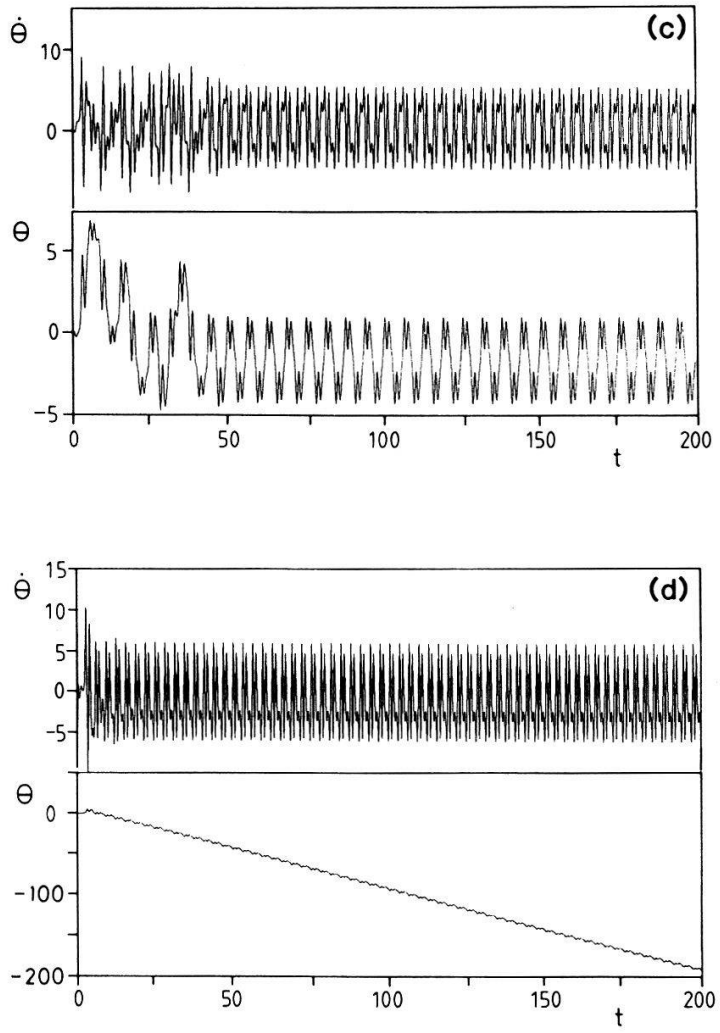

Figure 13

(*contd.*)

representative plots are shown in Fig. 15. These show the effect of the choice of p on the reconstruction, as described in Section 4.2.3. For Fig. 15(a), $p \ll \tau$, which results in a severe compression of the attractor along the line $\theta(t+p) = \theta(t)$, while Fig. 15(c) shows that for $p \gg \tau$ the reconstructed attractor appears to fill completely the phase space. As may be ascertained by comparing Fig. 15(b) with Fig. 10, the attractor is faithfully reconstructed for $p \simeq \tau$.

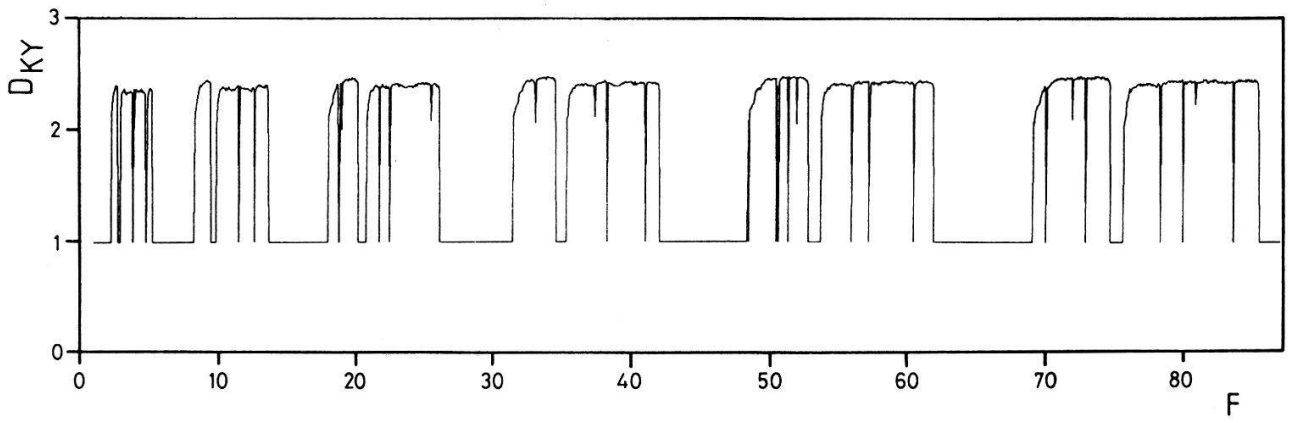

Figure 14

Dependence of D_{KY} on the amplitude of the driving force F.

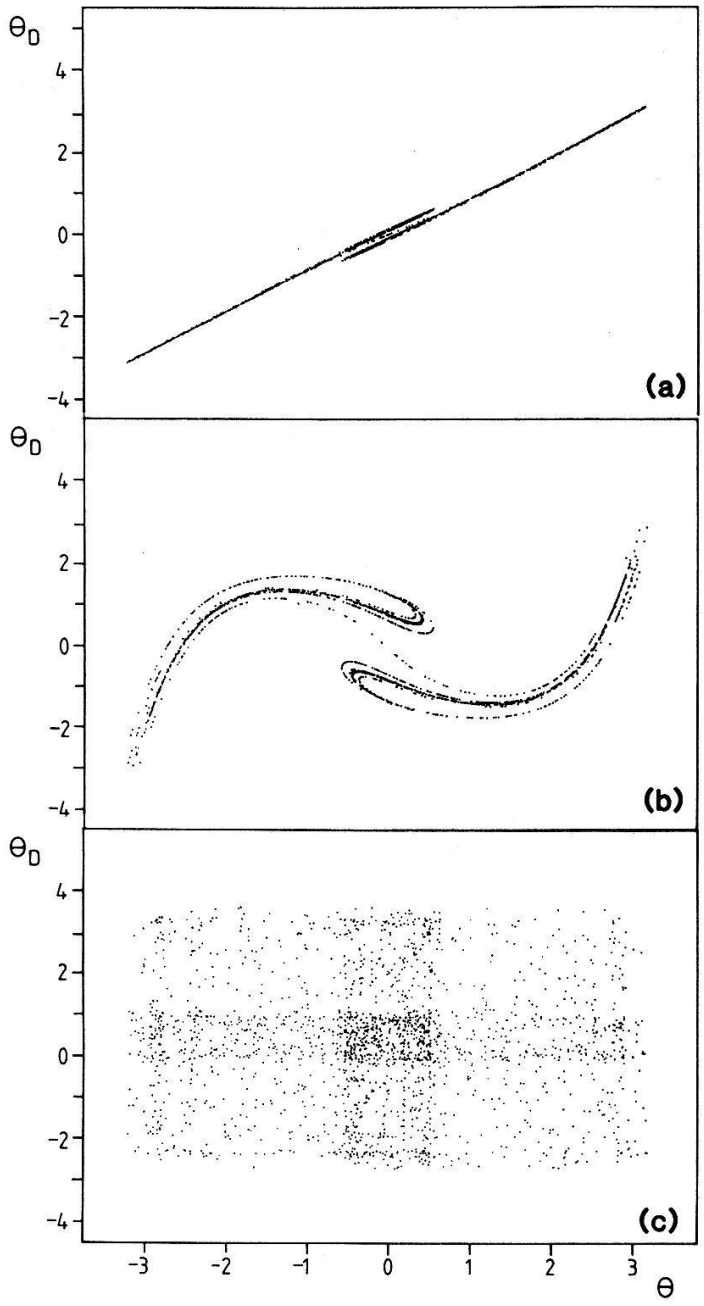

Figure 15
Reconstruction of the attractor for for a chaotic signal ($\Gamma = 0.4$, $F = 2.5$), for different choices of the time delay: (a) $p = 0.02\pi$ ($p \ll \tau$), (b) $p = 0.5\pi$ ($p \simeq \tau$) and (c) $p = 20\pi$ ($p \gg \tau$). To avoid transients, the points plotted correspond to the 2000 cycles following the first 10 cycles of the driving force.

6.5. *Correlation dimension*

The correlation dimension ν has been calculated for various parameter values (Γ, F) for which chaotic motion is observed. Although ν can be obtained from the attractor without the need of reconstruction, we have chosen to analyse, in general, reconstructed data in order to illustrate the usefulness of this procedure. In general, the time series $\Omega(t)$ was chosen for this study, since it displays a smaller low frequency component, and therefore can be represented more accurately by samples of restricted bit resolution. To conform with the

experimental data considered in Section 7, each record consisted of 8192 samples with 8 bit resolution.

Figures 16(a)–(c) show examples of logarithmic plots of $C(r)$ versus r, calculated for a data record with $\Gamma = 0.4$, $F = 2.5$ and a sampling interval of $t_s = 0.1$. Curves corresponding to three different values of the time delay are shown, namely, $p = 0.1$, 1, 10. Significant differences can be noted between the curves calculated for different values of p.

For both $p = 0.1$ and $p = 1$, the slope appears to saturate, with increasing embedding dimension m, over a large range of small r. However, the saturation value for $p = 0.1$ is 2.0 ± 0.1, whereas for $p = 1$ a value of 2.4 ± 0.1 is obtained. The correlation dimension calculated using the non-reconstructed attractor (with $N = 20{,}000$ and 10^{-16} precision) is $\nu = 2.28 \pm 0.05$, while the Hausdorff dimension using the Kaplan–Yorke conjecture is $D_{KY} = 2.35 \pm 0.02$. This fact suggests that the choice of $p \ll \tau$ has led to an under-estimate of the correlation dimension, due to a poor reconstruction of the attractor. We have found it to be generally true that for $p \ll \tau$, there is a slow convergence of slope necessitating the use of excessively large (for the given finite value of N_s) values of embedding dimension to obtain saturation. The resultant saturation value of the slope gives an unreliable estimate of the correlation dimension. It may be noted on comparing Figs. 16(a) and (b), that saturation occurs for $p = 1$ for $m \geqslant 4$, while for $p = 0.1$ saturation is observed only for $m \geqslant 8$.

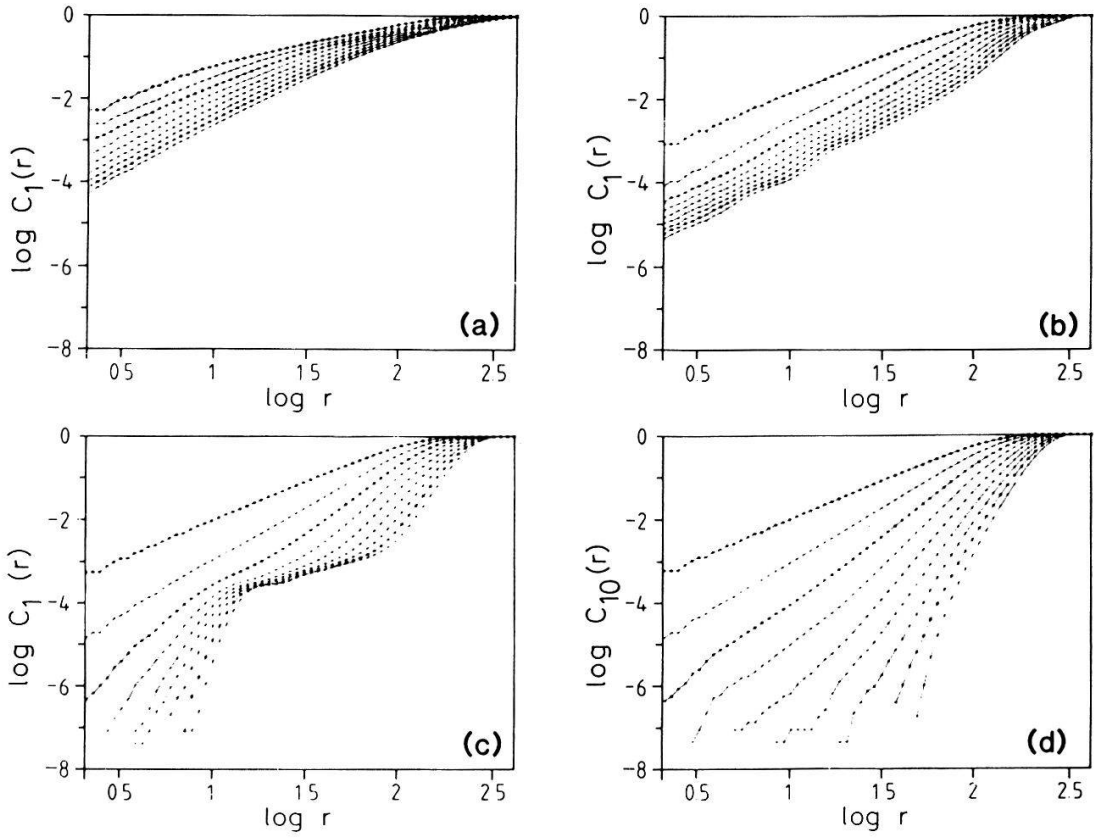

Figure 16
Logarithmic plots of $C_1(r)$ vs r ($\Gamma = 0.4$, $F = 2.5$, $t_s = 0.1$) for (a) $p = 0.1$, (b) $p = 1$ and (c) $p = 10$. For comparison, $C_{10}(r)$ vs r is plotted in (d) for the case $p = 10$, shown in Fig. 16(c).

For $p = 10$, Fig. 16(c) shows strong evidence of a plateau in $C(r)$ for a range of values of r. This feature is ascribed to the effect of 'spurious' correlations discussed in Section 4.2.5. This explanation is supported by the graph shown in Fig. 17. Plotted in this graph is the number of correlations N_{ij}, such that $|\vec{X}_i - \vec{X}_j| < r_0$ (for $m = 5$, $p = 10$ and $\log_{10} r_0 = 1.5$), versus the difference $|t_i - t_j|$ separating the times at which the first components of vectors $\vec{X}_i$ and $\vec{X}_j$ were recorded. If the attractor was sampled uniformly, N_{ij} should be linearly proportional to $N \cdot t_s - |t_i - t_j|$. However, Fig. 17 shows a highly disproportiate number of correlations N_{ij} for which $|t_i - t_j| < \tau$. This feature can be eliminated by considering the modified correlation integral defined in equation (4.3). A logarithmic plot of $C_{10}(r)$ versus r, calculated from the same data with $p = 10$, is shown in Fig. 16(d). The curves shown in this figure exhibit a linear relationship, even for the largest values of m considered. No saturation in slope is observable, however. This is consistent with the choice of $p \gg \tau$, as discussed in Section 4.2.3.

The effect of the choice of the sampling time has also been extensively studied. In general, t_s can be chosen within a wide range of values, with the correct value of ν being determined, provided an appropriate value of p is used. However, if $t_s \gg \tau$, then an excessively large value of p must be chosen, leading to a false value of ν. Conversely, if t_s is too small, the total sampling time $N_s \cdot t_s$ may not be sufficiently large to provide an adequate description of the attractor. In principle, the optimum choice for the sampling time t_s is a value less than τ, but greater than τ/m; provided, of course, that the dynamical system under study is statistically steady throughout the entire time interval during which data is being recorded.

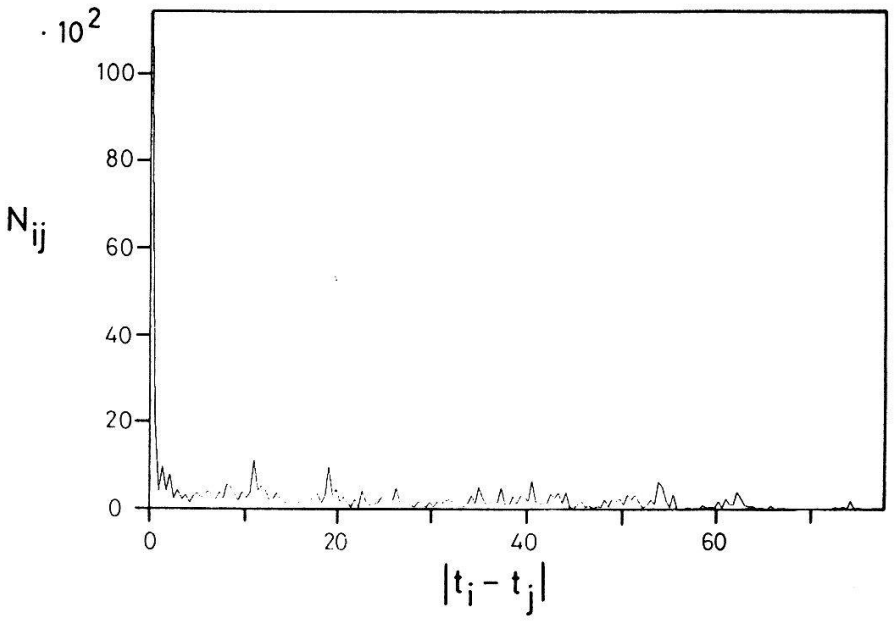

Figure 17
Number of correlation N_{ij} such that $|\vec{X}_i - \vec{X}_j| < r_0$ (for $m = 5$, $p = 10$ and $\log_{10} r_0 = 1.5$), versus the difference $|t_i - t_j|$ separating the times at which the first components of vectors $\vec{X}_i$ and $\vec{X}_j$ were recorded.

In conclusion, it should be stressed that an incorrect application of the Grassberger–Procaccia algorithm can lead to a false determination of the correlation dimension. We have found this to be particularly true if an attractor reconstructed from a single time series is considered. A judicious choice of parameter values, as discussed in Section 4.2, is essential for the correct value of ν to be determined.

7. Experimental study

7.1. *Apparatus*

An experimental model of the bipolar motor system [48, 49] has been constructed. A small permanent magnet, with $\mu \approx 1.7\,\text{Amp} \cdot \text{m}^2$ and $I \simeq 6 \times 10^{-6}\,\text{kg} \cdot \text{m}^2$ was suspended in a linearly polarized magnetic field ($B_\omega \leqslant 0.03T$) created by passing an oscillating current through a pair of Helmholtz coils. The magnet was restricted to rotate in a direction orthogonal to its magnetic axis by a pair of roller bearings. A Hall probe was placed near the magnet with its axis perpendicular to the direction of polarization of the oscillating field. This gave a measure of the position of the magnet $\sim\cos\theta$ (although, since the magnet produces an imperfect dipole field, higher order harmonics were also apparent in the measurements). A small pick-up coil was placed at $\theta = 180°$ relative to the Hall probe. This provided a measure of the velocity of the magnet $\sim\sin\theta \cdot \dot{\theta}$. A schematic diagram of the model is shown in Fig. 18.

For the measurements described here, the frequency of the oscillating field was fixed at $\omega/2\pi = 2\,\text{Hz}$. The strength of the field, and therefore the torque exerted on the magnet, was varied by adjusting the amplitude of the oscillating current passing through the Helmholtz coils. The damping of the motion of the

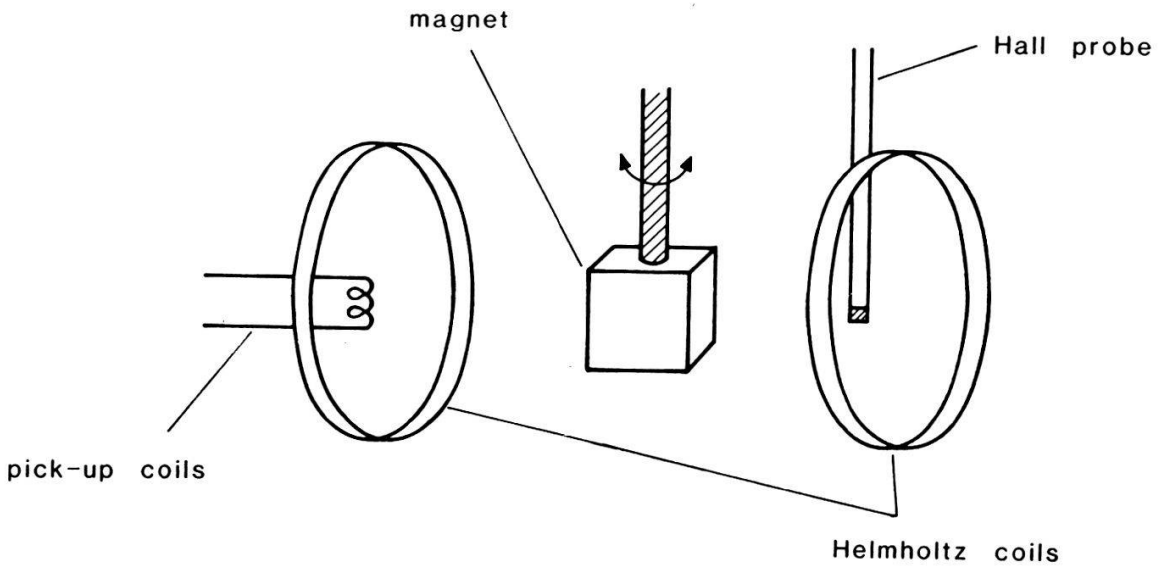

Figure 18

Schematic diagram of the experimental model of the bipolar motor.

magnet was provided by the inherent friction in the roller bearings. Unfortunately, this friction may not be well modelled by a force proportional to $\dot{\theta}$ as assumed in equation (6.1). There exists a non-negligible static coefficient of friction in addition to the velocity-dependent component. Although this experimental model could be considerably refined, both in terms of the frictional damping and in terms of the quantities measured (direct measurements of θ and $\dot{\theta}$ would be preferable for comparison with the theoretical study of Section 6), it was found to be adequate for the illustrative purposes of the present work.

Data from the Hall probe and pick-up coil were digitized into records of 8192 samples, using a sampling frequency of 100 Hz and 8 bit resolution. Because of their nature, the signals from the pick-up coil (being rather 'spikey', with a concentration of values near zero) were not very amenable to accurate digitization with the limited bit resolution available. We shall therefore concentrate our discussion on the analysis of results from the Hall probe, these being sufficient for the application of the Grassberger–Procaccia algorithm.

7.2. *Time series data*

Figure 19 shows the signals recorded by the Hall probe, after the decay of transients, for eight of the ten different values of the strength of the driving force F considered. These signals demonstrate that the experimental system has a behaviour that is qualitatively similar to that of the mathematical solutions described in Section 6. For example, the motion of the magnet is periodic (with the same period as the driving force) for $F = 16$; period doubled for $F = 6.4$; and chaotic for $F = 25.6$.

A more quantitative comparison for the bipolar motor system may be obtained by examining the values of F for which the different types of motion are observed. Analysis of the unforced motion of the magnet after an initial impulse gives an estimation of $\Gamma = 0.4 \pm 0.1$. Thus direct comparison of the experimental results with the calculations of Section 6 are possible. It should be noted, however, that due to imperfections in the experimental system (for example, slight drifts in the amplitude of the oscillating current passing through the Helmholtz coils), it should be expected that the fine structure of Fig. 11 will not be observable. (See Ref. [50] for a discussion of the effect of noise on the behaviour of the Logistic map.)

Comparing the behaviour of the experimental system shown in Fig. 19 with that predicted by the Lyapunov exponents plotted in Fig. 11, a rather close association of the presence of periodic and chaotic motions can be made. In particular, all (except two) values of F for which the experiment shows periodic/chaotic motion fall into calculated periodic/chaotic bands. The periodic motion observed for $F = 16$ is single-period rotation, while for $F = 6.4$ and 35.2 is period-doubled vibration, in agreement with Fig. 11 as discussed in Section 6.

7.3. *Correlation dimension*

The correlation integral has been calculated from the experimental traces of $\cos\theta$ for those values of F for which the motion of the bipolar motor was chaotic.

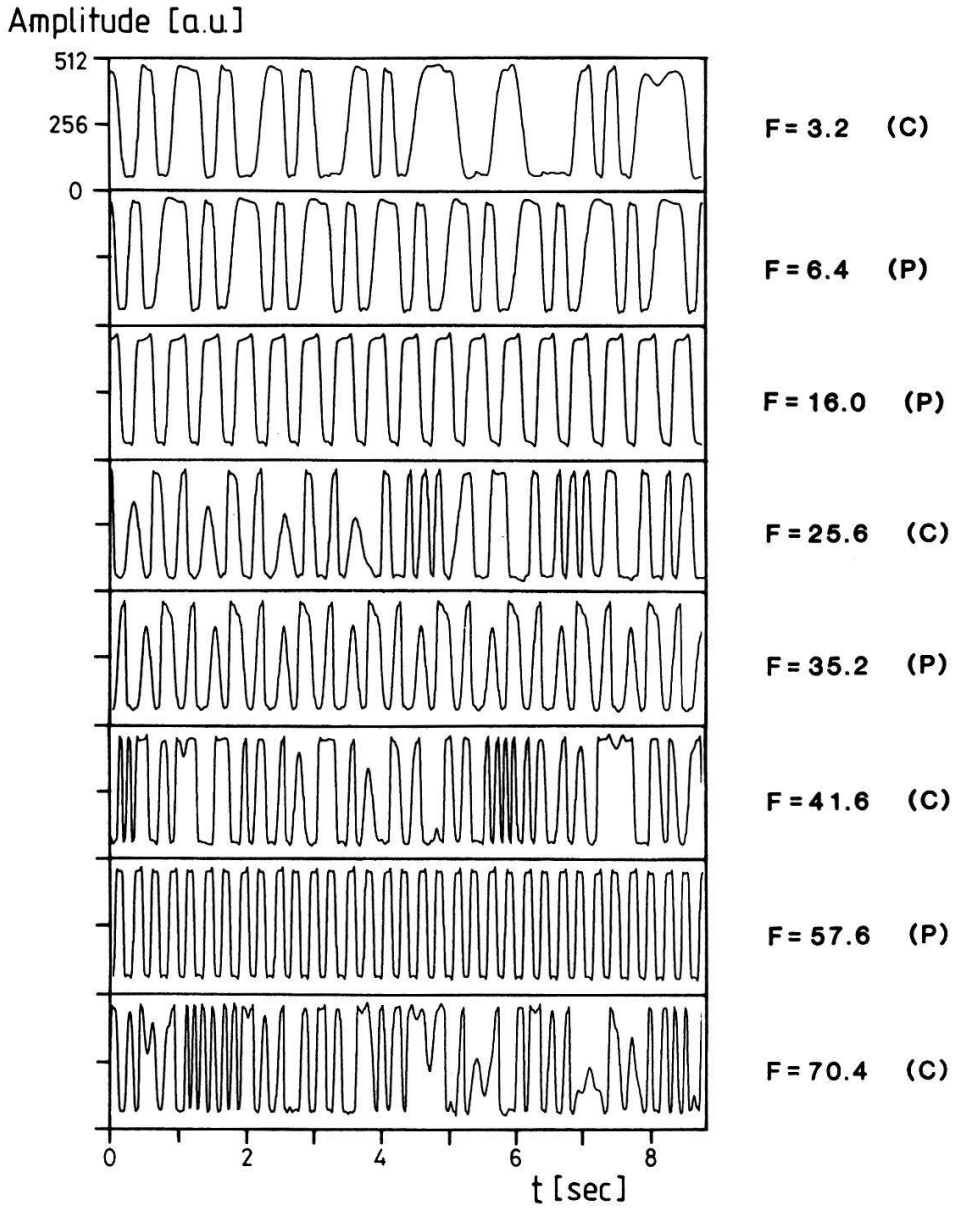

Figure 19
Signals recorded by the Hall probe ($\cos\theta$), for eight values of F, showing periodic (P) and chaotic (C) behaviour.

Logarithmic plots of $C(r)$ versus r are shown in Fig. 20 for three representative values of F. Saturation of the slopes for increasing embedding dimension m can be observed. Table II shows the values of the correlation dimension ν calculated from the experimental data for several values of F. Also shown in Table II are theoretical values of the correlation dimension and of the Hausdorff dimension calculated using the Kaplan–Yorke conjecture.

7.4 *Conclusions*

In making the comparison between theory and experiment for the bipolar motor some hopefully general features have emerged. Even with a crude experimental realization and an idealized theory (at least regarding damping) the qualitative agreement is good, not only concerning the types of motion observed but also concerning the values of the forcing parameter for which they are observed (particularly for small F).

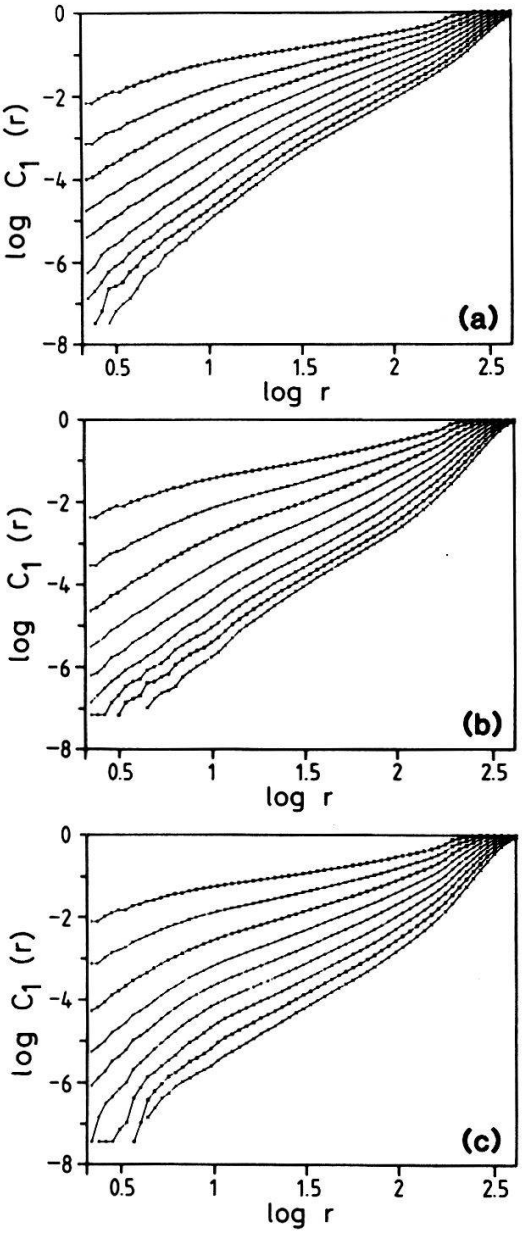

Figure 20
Logarithmic plots of $C_1(r)$ vs r for (a) $F = 3.2$, (b) $F = 25.6$ and (c) $F = 70.4$.

Table II
Experimentally and theoretically determined values of the correlation dimension ν, and the Hausdorff dimension D_{KY}, calculated for the bipolar motor with different values of F. The values of ν_{th} have been determined from a non-reconstructed attractor using $N = 20{,}000$.

F	ν_{exp}	ν_{th}	D_{KY}
3.2	2.5 ± 0.3	2.29 ± 0.08	2.36
26	2.6 ± 0.3	2.39 ± 0.07	2.41
42	2.9 ± 0.3	2.42 ± 0.08	2.42
48	2.5 ± 0.3	1.0	1.0
70	2.6 ± 0.3	2.43 ± 0.11	2.40
80	2.2 ± 0.3	2.35 ± 0.14	2.44

The dimensions calculated from the experimental data are reasonably close to the values obtained from numerical data, except where there is disagreement on the type of motion. This introduces the main hazard of a comparison, namely the sensitive dependence of the dynamics on the control parameters. From Fig. 11 it is evident that the Lyapunov exponents are very sensitive to changes in F. Nevertheless, as in a graphic representation of finite resolution, the general regions of chaotic and regular motion are evident. It is not clear as yet just how precise and constant system parameters need to be before detailed comparison is possible. However, the present study has shown that it is possible, with the available number of data points and resolution, to determine the correlation dimension of an experimental system if it is sufficiently small.

8. Analysis of broadband plasma fluctuations

In the following section, we examine the broadband fluctuations arising in a tokamak plasma.

A tokamak is a toroidal plasma confinement device in which the plasma is produced and heated by a toroidal current, and maintained in a toroidal magnetic field. This produces a closed confinement well, formed of magnetic field helixes located on concentric magnetic flux surfaces.

The experimentally measured confinement properties of such a structure are by a factor 50 to 100 times lower than expected from classical diffusion processes. The plasma is subject to instabilities, evidenced by the measured turbulent fluctuations, which are believed to be the cause of the degradation of confinement [51].

At the lower frequencies, typically in the kilohertz range, a tokamak discharge exhibits coherent fluctuations ($\Delta\omega/\omega \ll 1$) which are mainly due to large-scale helical structures undergoing a global rotation. This type of activity, usually called Mirnov activity, has been extensively studied and is known to have essentially no effect on the measured confinement properties of the discharge, provided its amplitude remains small.

In this section, we will concentrate on the higher frequency broadband fluctuations, suspected to be linked with the observed confinement degradation [52]. Since a tokamak plasma is a system possessing a very large number of degrees of freedom, it is pertinent to ask whether the broadband fluctuations display any low dimensional behaviour. Any means of characterizing these fluctuations more specifically than by their spectral characteristics may provide clues to the underlying dynamics.

8.1. *The TCA tokamak*

TCA is a circular cross-section tokamak with a minor radius $a = 0.18$ m and a major radius $R = 0.61$ m [53, 54]. The data analysed here have all been obtained from ohmically heated plasmas, with the following typical parameters: toroidal

magnetic field $B_T = 1.5\,T$, plasma current $I_p = 120\,\text{kA}$, line-averaged electron density $\bar{n}_e = 3.10^{19}\,\text{m}^{-3}$ and electron temperature on axis $T_e(0) = 800\,\text{eV}$. The temporal evolution of a typical discharge is shown in Fig. 21. Three different diagnostics are employed to measure the broadband magnetic and density broadband fluctuations [55].

(i) Two triple magnetic probes, located 180° toroidally apart, one on the top, the other on the outer equator, measure the three components of the magnetic field in the shadow of the limiters. We examine here the poloidal field fluctuations $\dot{b}_\theta$.

(ii) A triple Langmuir probe, also placed in the shadow of the limiters, measures the local fluctuations in the scrape-off layer. The probe is located in the equatorial plane, toroidally opposite to the limiter [56, 57]. Both fluctuations of the ion saturation current $\tilde{i}_s$ and the floating potential $\tilde{V}_f$ have been analysed in the present study.

(iii) An imaging diagnostic based on the phase contrast method [58], yields line-integrated density fluctuations $\int \tilde{n}_e\, dl$ along selected vertical chords. The chords are selected by displacing the detectors in the image plane. To reduce the influence of the low-frequency component of the fluctuations, these signals were filtered below 20 kHz.

The signals from each of the above diagnostics have been sampled in general at a frequency of 2 MHz, with a total number of data points $N_s = 8192$, and hence

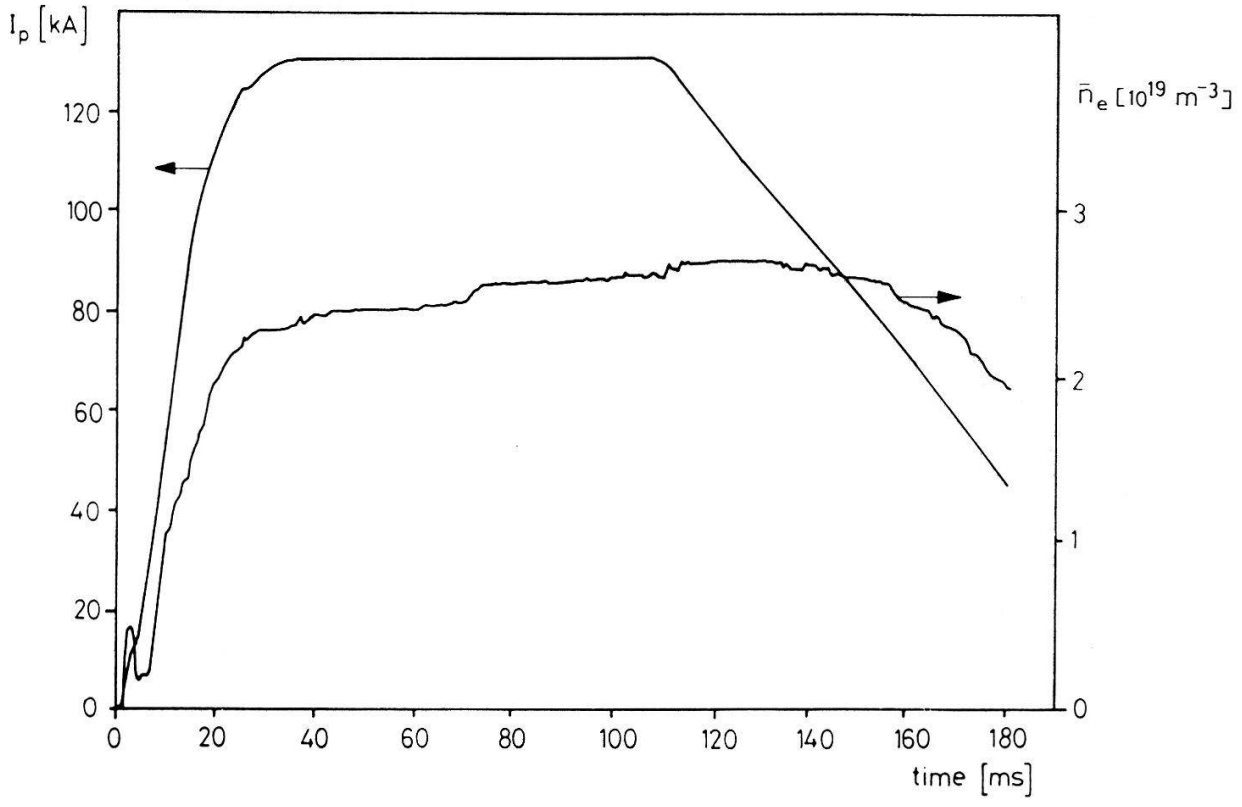

Figure 21

The temporal evolution of a typical discharge of the TCA tokamak.

a total sampling time ≈ 4 ms. This record length is short in comparison to the flat-top duration of TCA discharges, which lasts up to 150 ms.

8.2. *Raw data*

The correlation algorithm has been applied to all the signals mentioned above, even though in the following only four representative ones are shown: $\tilde{\dot{b}}_\theta$, $\tilde{i}_s$ and $\int \tilde{n}_e \, dl$ in discharges without a significant level of Mirnov oscillations, and for comparison, $\tilde{\dot{b}}_\theta$ in discharges exhibiting measurable Mirnov activity. The data were recorded for a variety of TCA discharges, over a wide range of plasma conditions and at different times during the discharge.

Figure 22 shows the first 500 μs of the time behaviour of each of the above signals, acquired during the current flat-top of the discharge. The low frequency oscillations associated with the Mirnov activity are clearly visible in the second trace. In the $\tilde{i}_s$ signal, a significant low-frequency component is noticeable, being due to the good low-frequency response of the Langmuir probe system.

The power spectra of these signals, shown in Fig. 23, are all extremely broad, with no indication of the presence of well-defined high-frequency peaks. In Fig. 23(b), the low-frequency Mirnov oscillation peak is clearly visible, whereas the effect of the high-pass filter at 20 kHz on the $\int \tilde{n}_e \, dl$ signal is seen in Fig. 23(c).

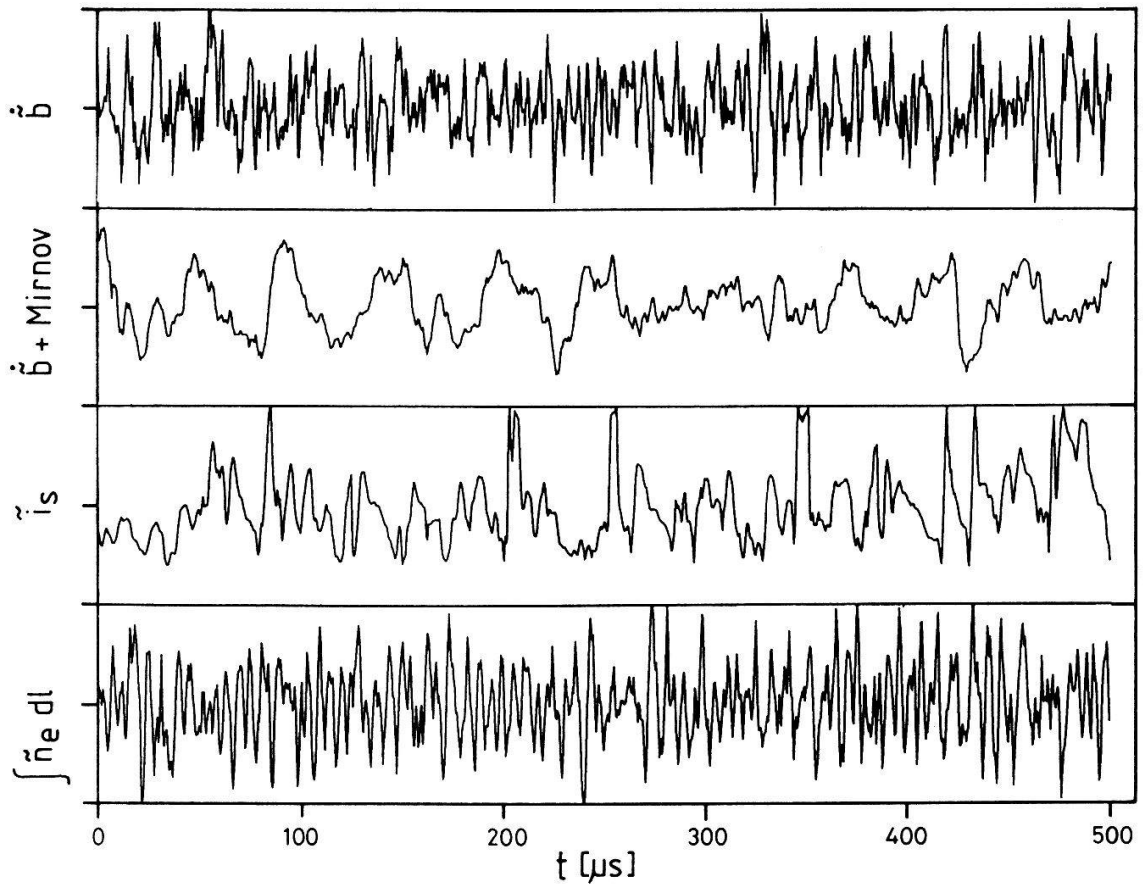

Figure 22
First 500 μs of the measured signals for fluctuations in poloidal magnetic field $\tilde{\dot{b}}_\theta$ (a) without and (b) with a significant level of Mirnov activity, (c) ion saturation current $\tilde{i}_s$ and (d) chord-averaged density $\int \tilde{n}_e \, dl$.

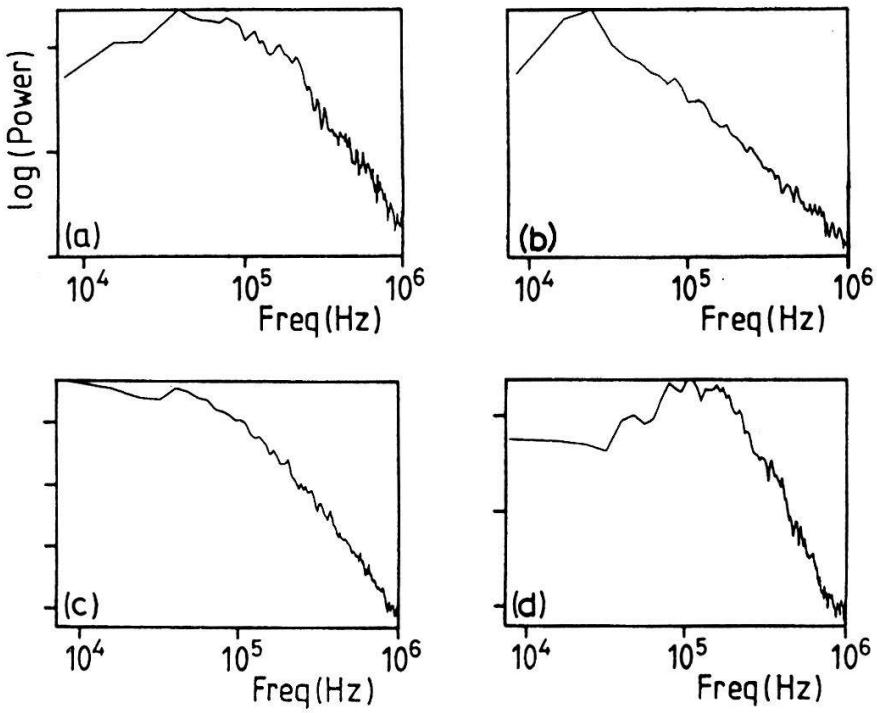

Figure 23

Power spectra of (a) $\dot{\tilde{b}}_\theta$, (b) $\dot{\tilde{b}}_\theta$ with Mirnov, (c) $\bar{i}_s$ and (d) $\int \tilde{n}_e \, dl$.

8.3 *Correlation dimension*

As measured from the autocorrelation function, the characteristic time τ of these fluctuation signals is rather short, about 2–5 μs. For the construction of the required m-dimensional vectors, a time delay of $p = 2\,\mu$s was therefore generally chosen for signals obtained from magnetic probes and the phase-contrast diagnostic. A larger value, for example $p = 5\,\mu$s, appeared more suitable for Langmuir probe data, and for magnetic probe data obtained from discharges with a measurable level of Mirnov activity, due to the larger low-frequency component in these signals.

Figure 24 shows the logarithmic plots of $C_1(r)$ versus r for embedding dimension $2 \leqslant m \leqslant 12$, for the above signals. Due to the finite value of N_s, it was observed that for $m > 10$ there does not exist a significant range of r for which the slope of $C_1(r)$ vs r is constant.

In Figs. 24(a) and (d), no evidence of saturation of the slope with m can be observed. However, Figs. 24(b) and (c), that is, $\dot{\tilde{b}}_\theta$ in a discharge with a significant level of Mirnov oscillations and the Langmuir probe data, exhibit evidence of a plateau for increasing values of m. The differences between the $C_1(r)$ vs r plots for the various signals are a consequence of the differences in the level of the low-frequency component of the signals.

It may be shown that the origin of the observed plateau are the spurious correlations mentioned in Section 4.2.5. To illustrate this fact, it is appropriate to consider $C_k(r)$ with $k \geqslant 5$. Figure 25 shows the logarithmic plots of $C_{10}(r)$ versus r, for the same data as used in Fig. 24. There is clearly no saturation in slopes for

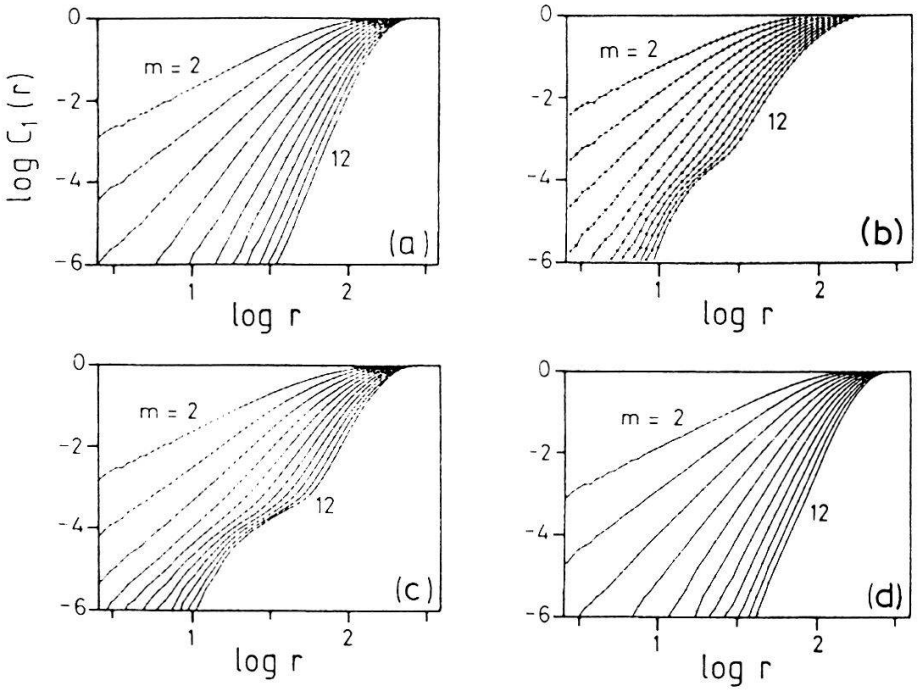

Figure 24
Logarithmic plot of $C_1(r)$ vs r for (a) $\dot{\tilde{b}}_\theta$, (b) $\dot{\tilde{b}}_\theta$ + Mirnov, (c) $\tilde{i}_s$ and (d) $\int \tilde{n}_e\, dl$.

increasing values of m for any of the signals. This is confirmed by Fig. 26, in which is plotted a graph of the slope of $\log C_{10}(r)$ vs $\log r$, as a function of m, for the magnetic probe data without significant Mirnov level. The slope is equal to the embedding dimension up to the largest value of m considered. Similar behaviour is observed for the other data.

The same analysis has been performed on signals recorded at different times

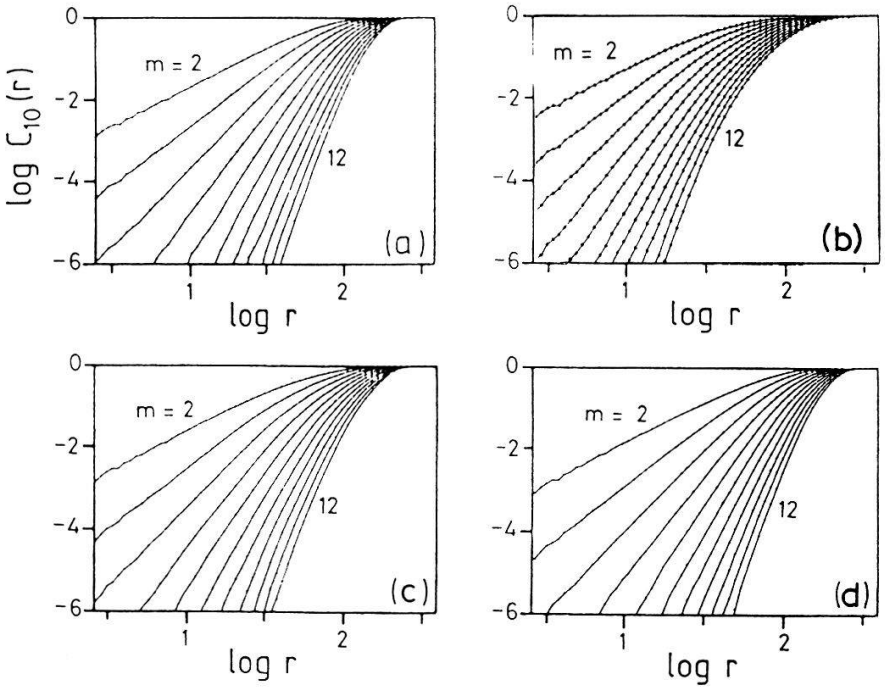

Figure 25
Logarithmic plot of $C_{10}(r)$ vs for (a) $\dot{\tilde{b}}_\theta$, (b) $\dot{\tilde{b}}_\theta$ + Mirnov, (c) $\tilde{i}_s$ and (d) $\int \tilde{n}_e\, dl$.

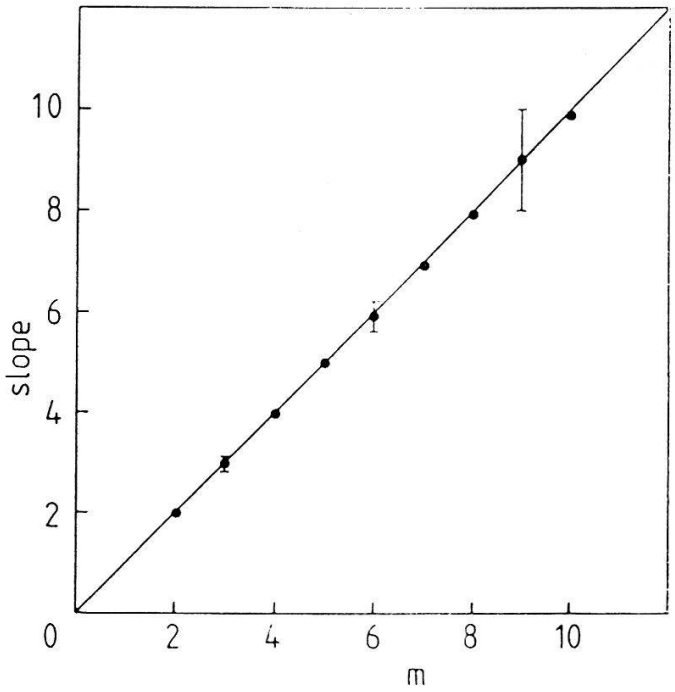

Figure 26
Slope of log $C_{10}(r)$ vs log r as a function of the embedding dimension m, for $\dot{b}_\theta$ as shown in Fig. 25(a).

during the current flat-top, as well as during the ramp-up phase of the plasma current. For none of the large sample of data was any clear indication of saturation observed.

In addition, studies have been undertaken to investigate the effect of the choice of sampling time. Fluctuation data were recorded, with $t_s = 2^{\alpha-5}\,\mu$s, $\alpha = 0, \ldots, 6$, maintaining the same value of $N_s = 8192$ and the same sampling start time in the discharge. For most of the values of t_s considered, similar results to those presented above were obtained, provided that the effect of spurious correlations was recognized and avoided. However, for the shortest sampling time (corresponding to a sampling frequency of 32 MHz), the number of available data points was too restricted to yield any finite region of r for which the slope of $C(r)$ versus r was constant. These observations are in accordance with the choice of the optimum value of t_s discussed in Section 6.5. Thus, contrary to the results of other workers [59], no evidence for a measurably low value of ν has been observed by utilizing very short sampling times.

We therefore conclude, from the present study of broadband fluctuations in the TCA tokamak, that there is no evidence for an attractor of low dimension [55, 60, 61]. Preliminary studies by other workers [62, 63] have shown indications of similar behaviour.

8.4. *Conclusions*

There exist two basic interpretations of the results obtained from the analysis of the tokamak data. The first interpretation is that the broadband fluctuations are associated with a high-dimensional system, $\nu > 10$ for the

available resolution. This suggests that the fluctuations result from a system having a large number of degrees of freedom. This is in agreement with the traditional picture of plasma turbulence [51]. The observation of extremely broad fluctuation spectra, with no coherent modes at frequencies above that of the Mirnov oscillations and their low order harmonics, is consistent with this interpretation.

An alternative interpretation is that the fluctuations are associated with a transient system (of either high or low dimension). It is not evident that the tokamak is in an equilibrium state (despite the constancy of all the measured quantities) during the sampling of the fluctuations. The algorithm for calculating the correlation dimension assumes that transients have decayed before the data are acquired. The dimensional analysis of such a transient system would be meaningless.

9. Conclusion

The goal of determining a non-linear model from the observation and analysis of chaotic dynamics is clearly a long way off. Nevertheless, it is evident that the application of correlation dimension analysis to experimental data is possible despite the complications introduced by sampled data and extrinsic noise. The bipolar motor and tokamak fluctuation dynamics have surprisingly similar Fourier spectra (with a change of frequency scale), but are readily distinguished by their correlation dimension. For the bipolar motor, a degree of comparison between theory and experiment was found possible despite the approximate nature of the model.

However, it has become clear that considerable care is required in the application of the Grassberger–Procaccia algorithm. Not only the parameters of the algorithm itself, but also those involved in the acquisition and reconstruction of an attractor often have a limited range of validity. These problems may be the cause of some of the diversity of results reported in the analysis of tokamak fluctuations. Recently, a thermodynamic formulation which provides a density $f(\lambda)$ of the continuous spectrum of exponents λ on the attractor has been found useful for application to experimental systems [67, 68]. Though related directly to the generalized dimensions, the $f(\lambda)$ curve may be more accessible from experimental data.

Acknowledgements

The authors would like to thank Ch. Hollenstein and H. Weisen for providing the fluctuation data from the Langmuir probes and phase contrast diagnostic. Discussions with A. Bondeson, J.-P. Eckmann and J. Vaclavik, as well as the reading of the manuscript by F. Yasseen are also gratefully acknowledged. This work was supported by the Fonds National Suisse de la Recherche Scientifique.

Appendix

The bipolar motor: transition to chaos

In Section 6.3, the Lyapunov exponents were calculated for the mathematical model of the bipolar motor, as a function of the amplitude of the driving force F. Figure 11 shows the existence of a series of values of F for which $\lambda_1 = \lambda_2 = 0$, at the beginning of each major band of chaos. These values, F_n^m, $n = 1, 2, \ldots, \infty$, for each band m, separate regions of increasing order of period doubling that the motion of the system exhibits during its transition to chaos.

Values of F_n^1, which precede the first band of chaos, are:

$$\begin{aligned} F_1^1 &= 1.892 \\ F_2^1 &= 2.256 \\ F_3^1 &= 2.30885 \\ F_4^1 &= 2.320155 \\ F_5^1 &= 2.322568 \\ F_6^1 &= 2.323091 \\ &\cdots \\ F_\infty^1 &= 2.323207 \end{aligned} \tag{A.1}$$

This series of numbers converge, i.e.,

$$\lim_{n\to\infty} \frac{F_n^1 - F_{n-1}^1}{F_{n+1}^1 - F_n^1} \equiv \delta = 4.68 \pm 0.05 \tag{A.2}$$

It is important to note that δ, called the Feigenbaum number [64], is a universal constant, its value being independent of the specific equations governing the period-doubling route to chaos.

REFERENCES

[1] J.-P. ECKMANN, Rev. Mod. Physics *53* (1981) 643.
[2] J.-P. ECKMANN and D. RUELLE, Rev. Mod Physics *57* (1985) 617.
[3] E. OTT, Proc. Int. Conf. Plasma Phys. (CRPP, Lausanne, 1984) vol. II, p. 817.
[4] R. SHAW, Z. Naturforschung *36a* (1981) 80.
[5] P. BERGÉ, Y. POMEAU and CH. VIDAL, in *L'ordre dans le Chaos*, Hermann, Paris 1984 (translation to be published by Wiley, New York, 1986).
[6] B. B. MANDELBROT, in *Les objects fractals*, Flammarion, Paris 1975, and in *The Fractal Geometry of Nature*, Freeman, New York, 1983.
[7] C. GREBOGI, et al., Physica *13D* (1984) 261.
[8] H. POINCARÉ, in *Les Méthodes Nouvelles de la Mécanique Céleste*, Gauthier-Villars, Paris 1892.
[9] E. N. LORENZ, J. Atmos. Science *20* (1963) 130.
[10] D. RUELLE and F. TAKENS, Comm. Math. Physics *20* (1971) 167.
[11] A. N. KOLMOGOROV, Dokl. Akad. Nauk. SSSR *124* (1959) 774.
[12] V. I. OSEDELEC, Trans. Moscow Math. Society *19* (1968) 197.
[13] J. D. FARMER, E. OTT and J. YORKE, Physica *7D* (1983) 153.
[14] H. G. E. HENTSCHEL and I. PROCACCIA, Physica *8D* (1983) 435.

[15] H. G. SCHUSTER, in *Deterministic Chaos,* Physik-Verlag, Weinheim 1984.
[16] C. E. SHANNON and W. WEAVER, in *The Mathematical Theory of Information,* Univ. of Illinois Press, Urbana 1949.
[17] J. BALATONI and A. RENYI, Publ. Math. Inst. Hung. Acad. Sci. *1* (1956) 9.
[18] P. GRASSBERGER and I. PROCACCIA, Phys. Rev. Letters *50* (1983) 346.
[19] D. RUELLE, Bol. Soc. Bras. Mat. *9* (1978) 83.
[20] Ya. B. PESIN, Usp. Mat. Nauk. *32* (1977) 55, and Russian Math. Survey *32* (1977) 55.
[21] J. KAPLAN and J. YORKE, in *Functional Differential Equations and Approximation of Fixed Points,* Lect. notes in Mathematics *730* (1979).
[22] D. A. RUSSEL, J. D. HANSON, and E. OTT, Phys. Rev. Letters *45* (1980) 1175.
[23] N. H. PACKARD, Phys. Rev. Letters *45* (1980) 712.
[24] F. TAKENS, Lect. notes in Mathematics *898* (1980) 366.
[25] Y. TERMONIA, Phys. Rev. A *29*(1984) 1612.
[26] A. COHEN and I. PROCACCIA, Phys. Rev. A *31* (1985) 1872.
[27] P. GRASSBERGER and I. PROCACCIA, Phys. Rev. A *28* (1983) 2591.
[28] A. WOLF and J. SWIFT, in *Statistical Physics and Chaos in Fusion Plasmas,* Horton & Reichle ed., Wiley, New York 1984 and A. WOLF et al., Physica *16D* (1985) 285.
[29] M. SANO and Y. SAWADA, Phys. Rev. Letters *55* (1985) 1082.
[30] J. WRIGHT, Phys. Rev. A *29* (1984) 2924.
[31] J.-P. ECKMANN et al., Phys. Rev. A (to appear).
[32] F. TAKENS, Lect. notes in Mathematics *1125* (1984) 99.
[33] H. S. GREENSIDE et al., Phys. Rev. A *25* (1982) 3453.
[34] P. GRASSBERGER and I. PROCACCIA, Physica *9D* (1983) 189.
[35] R. MAÑÉ, Lect. notes in Mathematics *898* (1981) 230.
[36] J. THEILER, Phys. Rev. A *34* (1986) 2427.
[37] P. ATTEN et al., J. Mécan. Théor. et Appliquée, numéro spécial 1984, p. 133.
[38] B. MALRAISON et al., J. Physique – lettres *44* (1983) L-897.
[39] M. HÉNON, Comm. Math. Physics *50* (1976) 69.
[40] E. OTT, Rev. Mod. Physics *53* (1981) 655.
[41] A. BEN-MIZRACHI et al., Phys. Rev. A *29* (1984) 975.
[42] R. BADII and A. POLITI, Proc. Workshop on Dimensions and Entropies (Los Alamos 1985), p. 67.
[43] I. SHIMADA and T. NAGASHIMA, Prog. Theor. Phys. *61* (1979) 1605.
[44] G. BENETTIN, L. GALGANI and J.-M. STRELCYN, Phys. Rev. A *14* (1976) 2338.
[45] H. HAKEN, Phys. Letters *94A* (1983) 71.
[46] J. P. CRUTCHFIELD et al., Phys. Letters *76A* (1980) 1.
[47] O. E. RÖSSLER, Phys. Letters *57A* (1976) 397.
[48] V. CROQUETTE and C. POITOU, C.-R. Acad. Sc. Paris *292*/series II (1981) 1353.
[49] V. CROQUETTE, Pour la Science (Décembre 1982), p. 62.
[50] J. P. CRUTCHFIELD et al., Phys. Reports *92* (1982) 45.
[51] P. C. LIEWER, Nucl. Fusion *25* (1985) 543.
[52] P.-A. DUPERREX et al., Phys. Letters *106A* (1984) 133.
[53] A. D. CHEETHAM et al., Proc. 11th Symp. on Fusion Technology (Pergamon, Oxford, 1980) p. 601.
[54] TCA Team, Nucl. Fusion *25* (1985) 1041.
[55] CH. HOLLENSTEIN et al., Proc. 13th Europ. Conf. on Contr. Fusion and Plasma Heating, Schliersee (EPS, Geneva, 1986), Vol. I, p. 144.
[56] A. de CHAMBRIER et al., J. Nucl. Materials *128 & 129* (1984) 310.
[57] CH. HOLLENSTEIN, Y. MARTIN and W. SIMM, Proc. 7th Int. Conf. on Plasma Surf. Interactions in Contr. Fus. Devices, Princeton 1986 (to appear in J. Nucl. Materials).
[58] H. WEISEN, Infrared Physics *25* (1985) 543 and H. WEISEN et al., Plasma Phys. and Contr. Fusion *28* (1986) 1161.
[59] H. J. BARKLEY et al., Report EUR-CEA-FC-1294/1986 (submitted to Pl. Phys. and Contr. Fusion).
[60] M. L. SAWLEY et al., Helv. Phys. Acta *59* (1986) 1070.
[61] M. L. SAWLEY, W. SIMM, and A. POCHELON, Phys. Fluids *30* (1987) 129.
[62] A. CÔTÉ et al., Proc. 12th Europ. Conf. on Contr. Fusion and Plasma Physics, Budapest (EPS, Geneva, 1985), Vol. II, p. 450.

[63] S. J. ZWEBEN et al., Proc. 7th Int. Conf. on Plasma Surf. Interactions in Contr. Fusion Devices, Princeton 1986 (to appear in J. Nucl. Materials).
[64] M. J. FEIGENBAUM, J. Stat. Physics *21* (1979) 669.
[65] J. D. FARMER, Z. Naturforschung *37a* (1982) 1304.
[66] Y. TERMONIA and Z. ALEXANDROWICZ, Phys. Rev. Letters *51* (1983) 1265.
[67] T. C. HALSEY et al., Phys. Rev. A *33* (1986) 1141.
[68] M. H. JENSEN et al., Phys. Rev. Letters *55* (1985) 2798.